Glass forming ability and crystallization behaviour of sub-alkaline silicate melts

Francesco Vetere[1-2-3], Gianluca Iezzi[1-4], Harald Behrens[3], Francois Holtz[3], Guido Ventura[4], Valeria Misiti[4], Andrea Cavallo[4], Silvio Mollo[4], Marcel Dietrich[3].

[1]Dipartimento di Ingegneria & Geologia, Università G. d'Annunzio, Chieti, Italy.

[2]Dipartimento di Fisica & Geologia, Università degli studi di Perugia, Perugia, Italy.

[3]Institute for Mineralogy, Leibniz University of Hannover, Hannover, Germany.

[4]Istituto Nazionale di Geofisica e Vulcanologia, Roma, Italy.

submitted to: Earth science review

corresponding author:

Francesco Vetere

Department of Physics and Geology,

University of Perugia

Piazza Università

06100, Perugia - Italy

Tel.: +39 075 585 2609

Fax : +39 075 585 2603

e-mail: francesco.vetere@unipg.it

ABSTRACT

The intrinsic solidification behaviour and glass forming ability (GFA) of natural sub-alkaline silicate melts have been quantified *via* cooling-induced solidification experiments. GFA is measured by the critical cooling rate *Rc*, the rate at which a melt solidifies ≤ 2 area% of crystals. Cooling rates of 9000, 1800, 180, 60, 7 and 1 °C/h have been run between 1300 °C (superliquidus region) and 800 °C (quenching temperature), at fO_2 and *P* of air for six silicate melts with compositions ranging from basalt (B) to rhyolite (R) (i.e., B_{100}, $B_{80}R_{20}$, $B_{60}R_{40}$, $B_{40}R_{60}$, $B_{20}R_{80}$ and R_{100}). The ranges of cooling rate and chemical composition are the broadest ever investigated in Earth Sciences.

The proportion of phases (area%) was determined by image analysis on about 500 back scattered electron images at different magnifications. Phases are glass, clinopyroxene (cpx), spinel (sp) and plagioclase (plg). Measured glass fractions correlate well with compositions of residual melts. Sp is the most ubiquitous phase with abundance of few area% and nucleates earlier than silicate crystals. Cpx solidifies in all liquids except in R_{100} and its abundance follows asymmetric broad Gaussian-like trends (with tails towards low rates) as a function of cooling rate. Moving from B_{100} to $B_{40}R_{60}$ these trends conserve their shape but shift progressively to lower cooling rates and abundances. Plg crystallizes only at low cooling rates and in SiO_2-poor compositions. Run-products with low amounts of crystals (≤ 5 area%) clearly show that cpx always preferentially nucleates on surfaces of sp, whereas a significant crystallisation of cpx (> 5 area%) is observed with decreasing cooling rates and with changing composition from B_{100} to $B_{20}R_{80}$. Thus, crystallisation of silicate crystals is related to the chemical diffusivity of components in the melt. Also the initial crystallization of plg occurs preferentially on cpx. In general, the amount of crystals decreases as the cooling rate increases; however, in some cases the amount of crystals does not increase or even decreases with the reduction of cooling rate for $B_{80}R_{20}$.

Rc values change over 5 orders of magnitude being < 1, 7, 620, 3020, 8020 and 9000 °C/h for R_{100}, $B_{20}R_{80}$, $B_{40}R_{60}$, $B_{60}R_{40}$ and $B_{80}R_{20}$ and B_{100}, respectively. Hence, the critical cooling rate strongly increases from R_{100} to $B_{80}R_{20}$, levelling off towards B_{100}. The variation of *Rc* can be modelled *via* NBO/T (non bridging oxygen per tetrahedron) parameter by the following equation:

Log Rc = a /{1+e$^{-[(NBO/T-b)/c]}$}, where *a*, *b* and *c* are fitting parameters equal to 3.814, 0.139 and 0.032, respectively. Similarly to other glass-forming liquids (network, metallic and molecular systems), the trend of *Rc* for natural sub-alkaline silicate melts is inversely related to the reduced glass transition parameter *T*rg (*T*rg = *T*g/*T*m) and can be quantified with the equation $Rc = a * Trg^{-b}$, where *a* and *b* are $1.19*10^{-4}$ and 28.7, respectively.

These results can be applied to retrieve the solidification conditions of aphyric, degassed and oxidised lavas; in addition, our data can be used to unravel general kinetic features of any solidifying natural silicate crystal-bearing (lavas with phenocrysts) melt erupted on Earth. The relationships between crystal content and cooling rate condition suggest that solidification paths induced by degassing can be also complex and not-linear. The grow of crystals with size up to 1 mm from a nearly anhydrous superheated silicate melt indicates that variable cooling conditions of lavas have to be accounted to correctly discriminate minerals formed before, during and after eruptions. Our results can be used to design glass-ceramics from easy to found and low cost starting materials.

1. INTRODUCTION

The glass forming ability (GFA hereafter) of many synthetic liquids has been extensively investigated in materials science (Uhlmann et al., 1979; Weinberg, 1996; Lu et al., 2000; Avramov et al., 2003; Cabral et al., 2003; Mondal and Murty, 2005; Fan et al., 2007; Zanotto, 2010; Guo et al., 2010; Gu et al., 2012); nevertheless, similar investigations have not been devoted to silicate glasses with chemical compositions common in nature, although the potential huge impact of the GFA parameter in Earth Sciences and, possibly, Materials Science. Several experimental studies have been reported in Earth sciences on the solidification induced by cooling but using few compositions (mainly basaltic) and within a relative restricted range of cooling rates and temperatures (Dowty, 1980; Lofgren, 1980; Kirkpatrick, 1981; Cashman, 1989; Lasaga, 1997; Hammer, 2008 for a general summary). The GFA summarises the intrinsic tendency to glassify or nucleate of crystals within a liquid; it reflects the most important transformation occurring on Earth, i.e. the transition from a silicate melt to a solid rock upon cooling. Any magmatic liquid either in subaerial or submarine environments, will form a glass if cooled sufficiently rapidly or will form a crystalline or partly crystalline body if cooled at slower cooling rates. Before an eruption, magmas mainly solidify by decompression-induced degassing (Applegarth et al., 2013) in conduits or by very sluggish cooling over thousands to millions of years in magmatic reservoirs (Whittington et al., 2009; Nabelek et al., 2012).

The lowest cooling rate that suppresses or strongly limits the nucleation of crystals is defined critical cooling rate (Rc hereafter); the amount of crystals for considering a material a glass is somewhat arbitrary (in many studies is considered 10^{-6} vol.%) and this implies that also Rc have to be referred to a crystal content defined *a-priori* (Shelby, 2005). Since the crystal content is determined by SEM observations, we cautionary define here glass a macroscopic solid material with ≤ 2 area% of crystals. Melts with low Rc persist in a metastable liquid state and have a high *GFA*. *Rc* of melts can be estimated using a) the reduced glass transition parameter $Trg = Tg / Tm$

(*Tg*, temperature of glass transition; *Tm*, temperature of melting), and b) the viscosity fragility notion (Lu et al., 2000; Fan et al., 2005 and 2007; Iezzi et al., 2009; Guo et al., 2010; Gu et al., 2012 and reference therein). A liquid with a low *Trg* and a high fragility has a low GFA, a high *Rc* (Fan et al., 2007; Gu et al., 2012) and tends to easily and rapidly nucleate.

This general reappraisal is qualitatively reflected by the solidification behaviour of natural silicate liquids (Iezzi et al., 2009; Vetere et al., 2013). SiO_2-rich (rhyolitic and trachytic) melts, with a low *Trg* and fragility, tend to easily vitrify or are reluctant to nucleate as temperature decreases (Swanson, 1977; Fenn, 1977; Naney and Swanson, 1980; Swanson et al., 1989; Sharp et al 1996; Sparks et al., 2000; Iezzi et al., 2008; 2011), whereas SiO_2-poor (basaltic) melts with high *Trg* and fragility easily nucleate and rapidly became rich in crystals (Dowty, 1980; Lofgren, 1980; Berkebile and Dowty, 1982; Fang et al., 1983, Cashman, 1991; Dunbar et al., 1993; 1995; Iezzi et al., 2009; Ray et al., 2010). However, a direct and systematic experimental approach to determine and quantify GFA *via Rc* of widespread natural silicate liquids and solidified rocks is still lacking.

GFA and *Rc* can be measured using several *ex-situ* and/or *in-situ* experimental and analytical methods (Fang et al., 1983; Weinberg et al., 1989; Ray et al., 2005; 2010; Shelby, 2005; Guo et al., 2010; Gu et al., 2012); the most used *ex-situ* approaches are based on the quantification of phases on run-products solidified by i) dynamic continuous cooling condition, where a liquid is cooled with a range of rates in a stepwise way until a glass is solidified or ii) the nose method based on the construction of TTT (time-temperature-transformation) diagrams obtained by static solidification experiments performed at several temperatures comprised between *Tg* and *Tm*. *In-situ* determinations of *Rc* instead basis on DSC (differential scanning calorimetry) and/or DTA (differential thermal analysis) measurements, that allows to determine further kinetic physico-chemical parameters; the most relevant is the temperature at the onset of crystallization *Tx*, on whom several GFA criterions rely (Ray et al. 2005 and 2010; Gu et al., 2012). Each of these approaches have both advantages and limitations; for instance, melts with a high *Rc* and/or a low exothermic crystallization peak can not be well investigated with DSC or DTA methodologies

(Shelby, 2005), whereas TTT diagrams requires a very long and tedious set of experiments; in fact, only a few TTT diagrams are available for natural silicate melts (Uhlmann et al., 1979; Lasaga, 1997), albeit their importance to bracket the variation of nucleation rates at different undercooling degrees. Finally, important information on the nucleation and crystallization behaviours related to cooling history of magma can be obtained using crystal size distribution studies (Cashman, 1989; Armienti et al., 1994; Lasaga, 1997; Higgins 2000 and 2006; Armienti, 2008).

In this study *Rc* and its evolution as a function of melt composition are derived *via* dynamic cooling experiments; indeed this approach is time consuming but has some advantages since dynamic cooling conditions simulate solidification behaviours pertinent to volcanic rocks on Earth and let to produce an experimental data set useful for the quantification of textural and compositional features of solidified phases. Here, we expand the experimental dataset of Vetere et al. (2013), allowing us to determine intrinsic *Rc* values of six liquid compositions along the basaltic-rhyolitic sub-alkaline join. At the same time, the intrinsic, complex and more relevant general solidification and crystallization behaviours of common silicate liquids can be deciphered. All the cooling-induced solidification experiments were initiated from the superliquidus region to fully homogenise these melts and remove as much as possible any foreign substrata potentially responsible for heterogeneous nucleation when a melt is cooled at the sub-liquidus region (Shelby, 2005, Vetere et al., 2013). Our cooling experiments end at relative low temperature (800 °C), when the glass transition region (viscosity ~ 10^{12} Pa s) is approached and the mobility of chemical components is negligible or very low.

The results attained here at ambient pressure and fugacity of air are relevant for the reconstruction or prediction of solidification conditions of many volcanic rocks solidified on the Earth surface; aphyric, degassed and oxidised lavas are the most comparable with our experimental data. Numerical simulations of conductive heat release of silicate melt layers with variable thicknesses allowed us to depict the natural conditions of cooling rates used in our experiments. Moreover, the models reported here for several chemical bulk liquid compositions can be useful to

design glass, glass-ceramic and holocrystalline materials based on abundant and low cost raw materials.

2. EXPERIMENTAL METHODS AND STRATEGY

2.1 Starting materials.

Six different silicate melt compositions along the sub-alkaline basalt-rhyolite join have been evaluated in this study. Their end-members are natural samples coming from Iceland (basalt) and Lipari Island in the Eolian arc (rhyolite). About 100 g of crushed natural basalt (B_{100}) and 100 g of crushed natural rhyolite (R_{100}) were melted in Pt crucibles in air at temperature of 1600 °C for 4 hours. After quenching on metal plates, glasses were crushed and re-melted at the same conditions to improve homogeneity.

The four intermediate compositions were obtained by mixing basalt and rhyolite glasses in the weight proportions (wt.%) 80:20 ($B_{80}R_{20}$), 60:40 ($B_{60}R_{40}$), 40:60 ($B_{40}R_{60}$), 20:80 ($B_{20}R_{80}$), respectively. The mixed powders were then synthesized at the same conditions reported above in order to ensure chemical homogeneity. Hence, we prepared six starting compositions with a systematic chemical variation reported in Table 1; these six starting materials correspond to basalt (B_{100}), basaltic andesite ($B_{80}R_{20}$), low- and high-evolved andesites ($B_{60}R_{40}$ and $B_{40}R_{60}$, respectively) dacite ($B_{20}R_{80}$) and rhyolite (R_{100}), as plotted in the TAS diagram (Fig. 1). Compositions of these starting glasses were determined by electron probe microanalyses (EPMA), H_2O content was measured by FTIR spectroscopy, and the density was calculated after Klöß, (2000); we calculated their *Trg* and NBO/T as thoroughly explained in Vetere et al. (2013) and summarised in Table 1.

2.2 Experimental strategy and techniques.

Large glass chips of several mm^3 were used for cooling experiments, in order to reduce as much as possible the ratio between glassy surfaces and their volumes; ~ 50 mg of these glass pieces

were loaded into Pt tubes that were squeezed and successively welded. A total of 10 experiments, 9 dynamic cooling experiments between 1300 °C to 800 °C plus one experiment quenched from 1300 °C directly to room temperature were run (Tables 2 and 3). Depending on the starting composition and on the experimental results from Vetere et al. (2013) based on cooling rates of 1800, 180 and 1 °C/h, three new further cooling rates of 9000, 60 and 7 °C/h were performed; SiO_2-rich compositions have a good GFA and thus experiments at high cooling rates are not necessary. Consequently fast cooling rates were considered only for SiO_2-poor compositions.

The used thermal paths are summarised in Table 2. All the experiments followed similar heating rate of 420 °C/h and dwell time of 1300 °C for 2 hours before quenching or rate of cooling (Table 2), except the experiment E-180a initiated at a higher temperature and using a longer dwell time (Table 2). Some experiments were also duplicated; note that the run-products duplicated at the same cooling rate of 1, 180 and 1800 °C/h were already characterised and discussed in Vetere et al. (2013). The cooling paths are displayed in Fig. 2, except the experiment with a more intense heat treatment before cooling (E-180a in Table 2). The whole time of dynamic cooling experiments thus ranges from a few hours (3.17) to about three weeks (510 hours), whereas the time of cooling is comprised between 3 minutes (9000°C/h) and 21 days (1 °C/h) (Table 2).

The experiments (E-180a, E-180b, E-60, E-7, E-1a and E-1b) with low cooling rates (180, 60, 7 and 1 °C/h) were run at the Dipartimento di Ingegneria & Geologia, University G. d'Annunzio of Chieti, (Italy), in a vertical rapid-quench Protherm PTF16/50/450 furnace at atmospheric pressure and air redox state. The temperature was monitored by two R-type ($Pt_{87}/PtRh_{13}$) thermocouples with accuracy ±3 °C. The internal thermocouple was directly in contact (< 1 cm) with the samples at the centre of the furnace, and the external thermocouple was positioned at the ceramic wall of the vertical furnace at the same height of the internal one. The thermal difference was less than 5 °C within the hot zone of the ceramic tube, which is a cylindrical zone with a length and diameter of about 2 cm. Quenching was achieved by dropping samples directly into a water bath at room temperature. The quenching time was less than 5 s.

The experiments (E-9000, E-1800a and E-1800b) at high cooling rates of 1800 and 9000 °C/h (Table 2) were conducted at the Institut für Mineralogie, Leibniz University of Hannover. Heating and cooling of the samples were performed using a high frequency generator (Linn[(R)], HTG 1000/1.3). The temperature was measured with a $Pt/Pt_{90}Rh_{10}$ (S-type) thermocouple 3 mm below the sample holder. The heating and cooling procedures were controlled with an Eurotherm[(R)] type 818 controller/programmer. Samples were placed directly in platinum capsules and sample holders. After closing the chamber (Behrens et al., 1996), the heating program was launched and cooling rate applied as soon as temperature was kept for 2 hours at 1300 °C. Quenching at 800 °C has been achieved by switching off the high frequency generator and rapidly taking out the sample holder and rolling it on a metal plate. The very high metal conductivity (Pt capsules in Pt sample holder) immediately dropped the temperature down to room temperature. Time required for this procedure was estimated to be ~ 5 s.

One experiment (E-quench) was performed by rapidly quenching the sample into water from 1300 °C after a dwell of 2h; this run was performed at Hannover, using a Gero-HTRV vertical furnace, in order to constrain chemical and textural features before the onset of cooling rates (Table 2). In this experiment, temperature was monitored with two S-type thermocouples, the first placed near to the wall of the ceramic tube and the second in contact with the samples. For this experiment samples were placed directly in platinum capsules and tied to a ceramic sample holder using a Pt wire. After running the heating program, and a dwell temperature of 1300 °C for two hours, capsules were quenched by falling down them in a water bath. Charges of E-quench experiment were cooled with a rate $\geq 10^5$ °C/h (Table 2).

3. ANALYTICAL METHODS AND IMAGE ANALYSIS

3.1 Analytical techniques.

After quench, all samples were mounted in epoxy, ground flat and polished to analyse all portions of run-products, comprised the interfaces between solidified charges and Pt capsule walls. Chemical and textural features were all determined on these polished sections. The composition of phases, i.e. starting glasses, glass matrix and crystalline phases of run-products were all analyzed using an electron microprobe (JEOL JXA 8200) or a JEOL FE-SEM 6500F equipped with an energy dispersive X-ray (EDX) microanalysis system, both installed at the HP-HT laboratory of Volcanology and Geophysics of Istituto Nazionale di Geofisica e Vulcanologia (Rome, Italy). The analytical conditions of EPMA and FE-SEM as well as data reduction used here are the same reported in Iezzi et al. (2008; 2011; 2014). Chemical characterisation of phases with a diameter between 1 and 3 μm was performed using FE-SEM, whereas phases with a size dimension > 3 μm were analysed by EPMA. The differences of average chemical compositions obtained by EPMA or FE-SEM was very low as evidenced by replicated analyses of the same glass matrix (Fig. 3).

3.2 Image analysis.

The textural features were analysed with FE-SEM using back-scattered electrons (hereafter BS). To accurately characterize the textures and the distribution of phases, as well as the possible tendency to nucleate and crystallize preferentially on Pt walls, images were collected at magnifications of 150×, 400×, 800×, 1500× and 3000×, with sizes of 600 x 800, 280 x 225, 155 x 95, 80 x 60 and 40 x 18 μm^2, respectively. Phases showing sub-micrometric features were also investigated using magnifications up to 50000x. For some run-products a high number (8 to 36) of adjacent images were collected to better evaluate the distribution of phases. As a whole, about 1000 FE-SEM images with section areas ranging between 10^0 to ~ 10^6 μm^2 were collected; about 500 of them, mainly at magnification of 150x, 400x and 800x, were used for the determination of phase content by image analysis.

The phase amount and their distribution (homogeneous *vs* inhomogeneous, see below) in each run-product were determined with the Image-ProPlus 6.0 software; the analytical protocol of

image analysis is the same reported in Iezzi et al. (2008; 2011), Lanzafame et al. (2013) and Vetere et al. (2013). For each run-product, the identification of phases was determined by linking their grey-level ranges with their chemistries; then, the area% fraction of each recognised phase was automatically counted. The abundance and estimated standard deviation of each phases was obtained on averaging from 3 to 36 images; the BS-SEM images (recorded in different parts of each sample), their magnifications and numbers used for the determination of phase content were selected as a function of the mean size of crystalline phases and their qualitative distribution previously evaluated at 150×, 400×, 800×, 1500× and 3000×. We did not apply a stereological correction, in order to avoid any mathematical manipulation of the data. We also re-analysed some run-products previously reported in Vetere et al. (2013).

4. RESULTS

4.1 Qualitative overview of textures.

The general textural features of run-products and their crystalline phases are shown in Figs. 4a, 4b and 4c as a function of cooling rate and bulk liquid composition. Phases detected and analysed in the run-products are mainly clinopyroxene (cpx), plagioclase (plg), spinel (sp) and glass; melilite, orthopyroxene and olivine occurred with a very low amount (< 1 area %) in a few SiO_2-poor run-products. Qualitatively, the amount and size of crystals increase and their number per area decreases as the cooling rate decreases for the same bulk composition or when the initial liquid composition shifts from R_{100} (especially from $B_{20}R_{80}$) to B_{100} at the same rate. R_{100} run-products have always very low crystal contents (Figs. 4a and 4b). In the whole data set, the crystal length ranges between 0.2/1 and 500/1000 μm; the tiniest crystals are spinels and the largest ones are plagioclases (Figs. 4b and 4c). The shape of crystals changes from dendritic (acicular interconnected branches *vs* fern leafs aspects) to skeletal/hollow to irregular/nearly faceted shapes; for B_{100}, $B_{80}R_{20}$, $B_{60}R_{40}$, $B_{40}R_{60}$ and $B_{20}R_{80}$ dendritic crystals occur at cooling rates > 180, > 60, >

60, > 1 and > 1 °C/h, respectively, while skeletal/hollow crystals solidify at cooling rates > 7, > 7 to > 1, and > 1 °C/h for B_{100}, $B_{80}R_{20}$ and $B_{60}R_{40}$, respectively (Figs. 4a and 4b). The aspect ratio (length/width) of crystals decreases as the cooling rate decreases for the same composition or when the initial liquid composition shifts from R_{100} (especially from $B_{20}R_{80}$) to B_{100} (Figs. 4a and 4b) for a constant cooling rate.

Sp, even if very tiny as in R_{100} run-products, crystallises with an equant shape and linear edges (Fig. 4c). Intergrowth of cpx and plg occurs at high crystallization degrees suggesting simultaneous solidification that mutually limited their grown (Figs. 4a and 4b; see also the discussion paragraph). Run-products with low crystal contents evidence that cpx solidified as acicular dendrites around sp crystals (Fig. 4b); cpx dendrites appear to grow along preferred crystallographic directions (Fig. 4b). In run-products with a low amount of plg, this phase crystallises on cpx rims (Fig. 4b).

4.2 Homogeneity of textures and preferential crystallization on Pt substrata.

A heat treatment of 2 hours at 1300 °C is able to re-homogenise our six starting liquids and eliminate as much as possible heterogeneous sites such as incompletely-melted crystals, bubbles, ghost boundaries. Thus, the phase assemblage obtained at 800 °C, after a defined cooling rate, can be ascribed to the intrinsic physico-chemical features of these liquids (Tsuchyama, 1983; Lesher et al., 1999; Vetere et al. 2013). Some textural criteria can be used to evaluate the reproducibility of run-products and if their features are affected by a thermal gradient (Vetere et al., 2013). These criteria include: i) variation of phase contents (and possibly sizes and shapes) on different portions of a each run-product, quantified by their standard deviations of area% and ii) tendency to crystallise on Pt substrata. In this work, run-products with a standard deviation of phase abundance < 4 area % are considered homogeneous and labelled *H*, inhomogeneous if > 4 area % and indicated as *IN*; the enrichment of phase proportion on Pt walls is labelled *P*, an absence of enrichment is instead indicated by *A* (Table 3).

Between two run-products cooled at the same rate, we consider for the following discussion only the most homogeneous ones (in bold in Table 3). In the absence of duplicated cooling experiments, we are forced to consider the E-1800 and E-7 for $B_{80}R_{20}$, E-7 for $B_{60}R_{40}$ and E-7 for $B_{40}R_{60}$ run-products although they are inhomogeneous (Table 3); however, only E-1800 and E-7 for $B_{80}R_{20}$ and $B_{60}R_{40}$, respectively, have high standard deviations and thus are unequivocally inhomogeneous (Table 3). Crystals in run-products B_{100}, $B_{80}R_{20}$ and $B_{60}R_{40}$ are more prone to crystallize on Pt-substrata; spinel is the crystalline phase that preferentially grows on Pt (Figs. 4a and 4b).

4.3 Crystal contents and estimate of Rc.

The crystal content of each run-product is summarised in Table 3 and its evolution for each chemical system and cooling rate is displayed in Fig. 5. Despite the qualitative and general observations provided by FE-SEM micro-photographs (Figs. 4a, 4b and 4c), we found complex trends, i.e., the crystal content increases, remains constant or even decreases with decreasing cooling rate (Fig. 5). There are only two crystal-bearing R_{100} run-products (Table 3) and thus a clear trend cannot be defined for this bulk composition. In general, the crystal content increases as the cooling rate decreases for B_{100}, $B_{60}R_{40}$, $B_{40}R_{60}$ and $B_{20}R_{80}$. In detail, for each composition, there are sub-horizontal portions in the trends of Fig. 5. However, even if the crystal content does not change, crystals in these run-products show different size and shape as a function of cooling rate (Figs. 4a, 4b and 5). Intriguingly, $B_{80}R_{20}$ run-products show an increasing (7-180 °C/h) and a decreasing (1-7 and 180-9000 °C/h) crystal content as a function of cooling rate (Fig. 5). Only B_{100} run-product is completely crystallised at cooling rates ≤ 60 °C/min and the crystal content suddenly decreases from 1800 to 9000 °C/h (Fig. 5). The cooling rates of B_{100}, $B_{80}R_{20}$, $B_{60}R_{40}$, $B_{40}R_{60}$ and $B_{20}R_{80}$ liquids with 2 area% of crystals are 9000, 8020, 3020, 620 and 7 °C/h as estimated in Fig. 5. We infer that these *Rc* values have an accuracy better than 10% Therefore, these cooling rates represent

the Rc of the bulk compositions; the 2 area% of crystals for R_{100} run-products is estimated to be lower than 1 °C/h, thus we approximate Rc of R_{100} to 1 °C/h (Fig. 5).

4.4 Sp, cpx and plg crystallisation behaviours.

The crystallisation behaviours of sp, cpx and plg as a function of cooling rate are displayed in Fig. 6. Due to the oxidized conditions of the experiments, sp crystallizes in all runs with exception of the most SiO_2-rich compositions at high cooling rates. The abundance of sp increases from B_{100} to $B_{20}R_{80}$; sp is the only crystalline phase in the R_{100} run-products (up to 1.5 area%, E1-b in Table 3). Its maximum amount is 5.4 area% (experiment E-180b) in the B_{100} (Table 3 and Fig. 6). Trends of cpx contents have an asymmetric broad Gaussian-like shape with a long tail towards low rates of cooling in bulk compositions B_{100} - $B_{40}R_{60}$, since cpx content first increases moderately and then suddenly decreases as the cooling rate increases. These trends are progressively shifted towards lower cooling rates and crystal contents as the bulk chemical composition changes from B_{100} to $B_{40}R_{60}$ (Fig. 6). In $B_{20}R_{80}$ only a steep decreasing trend is observable (Fig. 6). In the whole data set, the maximum amount of cpx is beyond 50 area % in B_{100}. For the same cooling rate, the amount of cpx decreases from B_{100} to $B_{20}R_{80}$ (Table 3 and Fig. 6). Plg, instead, crystallizes only from B_{100} to $B_{40}R_{60}$ and at lower cooling rates. In the homogeneous $B_{40}R_{60}$ run-product the plg content is very low (Table 3 and Fig. 5); in B_{100} and $B_{60}R_{40}$, plg show monotonically decreasing trends and disappears at cooling rates > 180 and > 60 °C/h, respectively. In $B_{80}R_{20,}$ the plg trajectory is very different due to a strong decreasing content from 1 to 7 °C/h (Table 3 and Fig. 6).

The appearance of silicate crystals as a function of cooling rate and bulk composition has been also estimated by considering the amount of 2 area % of cpx in our data set in Fig. 6. From B_{100} to $B_{20}R_{80}$ (Fig. 6) cpx starts to nucleate at about 8880, 7900, 2150, 450 and 6 °C/h, respectively. The cooling rate necessary to nucleate cpx mirrors that of sp as a function of the liquid composition (Figs. 5 and 6), since it slightly decreases from B_{100} to $B_{80}R_{20}$, then strongly decreases of two orders of magnitudes from $B_{60}R_{40}$ to $B_{20}R_{80}$ (Fig. 6). On the other hand, the crystallisation of

significant amounts of cpx of 10, 20 and 30 area % occur at about 7200, 5300 and 4000 °C/h for B_{100}, ~ 4900, 2600 and 1100 °C/h for $B_{80}R_{20}$ and around 1000, 400 and 180 °C/h for $B_{60}R_{40}$; for $B_{40}R_{60}$ rates of 180 and 60 °C/h are required to solidify 20 and 30 area % of cpx (Figs. 5 and 6). Hence, the abundant crystallisation of cpx is mainly imposed by the composition of the residual liquid.

4.5 Composition of glass.

The average compositions of glasses of the most homogeneous and crystal-bearing run-products (those in bold in Table 3), measured either by EPMA or FE-SEM (Fig. 3), are reported in Table 4; glasses analysed at least 50 μm away from crystals are termed matrix glass, whereas those in the first 50 μm from crystal edges are indicated as intracrystalline glasses (Table 4). Obviously, R_{100} glasses have compositions practically identical to the R_{100} bulk composition (Tables 1 and 4) due to its low crystal content. SiO_2 concentrations (wt.%) of matrix and intracrystalline glasses together with their five bulk compositions are displayed in Fig. 7 as a function of crystal content. A higher crystal content determines a nearly linear enrichment of SiO_2 in glasses quenched at 800 °C for B_{100}, $B_{40}R_{60}$ and $B_{20}R_{80}$ and a more scattered general trends for $B_{80}R_{20}$ and $B_{60}R_{40}$ (Fig. 7); as a whole, these trends evidence that area% phase abundances, determined by image analysis without any mathematical corrections, reflect the volumetric abundance of phases. However, the highly scattered trends of $B_{80}R_{20}$ and $B_{60}R_{40}$ evidence that the increase of crystals does not inevitably produce SiO_2 enrichments in the glass phase, when the composition of the residual glass is buffered by that of the crystals.

The behaviour of SiO_2 in glasses also indicates that, during crystallization, the residual melts approach to more evolved chemical compositions (Fig. 7). The most relevant are $B_{80}R_{20}$ and $B_{60}R_{40}$ attaining residual melt compositions more silicic than the bulk $B_{20}R_{80}$ liquid for a crystal content in excess of 50 area% (Tables 3 and 4 and Fig. 7). Furthermore, the only run-product with a high crystal content and the lack of SiO_2 enrichments is the $B_{80}R_{20}$ of E-1800 experiment (Table 3),

showing a crystal content of 25.6 area% and 53.9 (by EPMA) or 51.87 (by FE-SEM) wt.% of SiO_2 (Table 4) very close to the $B_{80}R_{20}$ bulk composition (Table 1 and Fig. 7). This indicates that the SiO_2 concentration of cpx, which was not analysed due to the very tiny size of crystals, is almost identical to that of the starting melt.

4.6 Cpx compositional variation.

In this study the compositions of cpx are reported only to corroborate and better interpret the textural results and thus only the most important and general features are presented here. An exhaustive treatment of crystal-chemical variations as a function of kinetic conditions will be performed in a future work, together with the chemical evolution of sp and plg, by thorough analyses of core-to-rim crystal compositions as shown in Mollo et al. (2010) and Iezzi et al. (2014). The mean oxide compositions of cpx in run-products are reported in Table 5. As the crystal content increases the average amounts of CaO and Al_2O_3 linearly decrease and increase, respectively (Fig. 8); except for the content of Al_2O_3 at 180 and 1800 °C/h in B_{100} and the content of CaO in $B_{60}R_{40}$, our data (Fig. 8) are consistent with results from alkaline and cal-alkaline liquids cooled at rates comparable to those used in this study (Mollo et al., 2010; 2012a).

5. DISCUSSION

The crystallisation behaviour of anhydrous natural silicate melts relies on previous cooling-induced dynamic crystallisation experiments either *ex-situ* (Gibb, 1974; Lofgren et al., 1974; 1979; 1986; Walker et al., 1976 and 1978; Bianco and Taylor, 1977; Lofgren, 1977; 1989; Grove and Raudsepp, 1978; Donaldson, 1979; Uhlmann et al., 1979; 1981; Corrigan, 1982; Fang et al., 1983; Kirkpatrick et al., 1981; 1983 Tsuchyama, 1983; Baker and Grove, 1985; Lesher et al., 1999; Burkhard, 2005; Conte et al., 2006; Faure et al., 2003; 2007; Pupier et al., 2007; Walton and Herd, 2007; Orlando et al., 2008; Hammer, 2009; Del Gaudio et al., 2010; Iezzi et al., 2008; 2011; Mollo

et al., 2010; 2011; Vona and Romano, 2013 and references therein) or in a few *in-situ* (Sunagawa, 1992; Schiavi et al., 2009; Ni et al., 2014) studies, reviewed in the last decades (Lofgren, 1980; Kirkpatrick, 1981; Cashman, 1989; Lasaga, 1997; Hammer, 2008; Zhang, 2008). However, with respect to the wider conditions presented in this study, results from previous experiments were based on more limited: i) ranges of temperatures (the onset temperature of cooling and quenching), ii) cooling rates, and/or iii) chemical compositions (chemistries like B_{100} and $B_{80}R_{20}$ were by far the most investigated). The use of six silicate liquids with a systematic chemical variation (Fig. 1) together with a very broad range of cooling rates from 1 (10^0) to 9000 (~10^4) °C/h between 1300 - 800 °C (Fig. 2) give a more general reappraisal of the intrinsic solidification behaviour of natural silicate liquids. Cooling rates slower than 1 °C/h are difficult to perform due to the very long experimental time required (> 3 weeks). Although the limitations due to the very sluggish nucleation behaviour of R_{100} composition, it is possible to quantify for the first time the intrinsic GFA (*via Rc*) and its dependence on the bulk chemistry (Figs. 5 and 6); moreover, it is possible to depict the most relevant solidification and crystallization trends of widespread silicate liquids on Earth and similar planets (Figs. 4a, 4b and 4c). The dataset presented here can be expanded by new experiments adequately designed to unravel the effects of pressure, volatile content, redox state, curvilinear rate, strain rate and presence of crystals and/or bubbles at the onset of dynamic cooling.

5.1 GFA vs liquid composition.

As aforementioned, *Rc* increases from R_{100} to B_{100} of almost five order of magnitudes, mostly over the effect of SiO_2 of the melt (Fig. 5). The bulk chemical variability of silicate liquids is commonly described by the number of non-bridging oxygens (NBO) per tetrahedrally coordinated cation (T) (Mysen and Richet, 2005), calculated as follows for our six silicate melts (Table 1):

$$\frac{NBO}{T} = \frac{1}{T} \cdot \sum_{i=1}^{i} n \cdot M_i^{n+}$$

(1)

where T is the total atomic abundance of tetrahedrally coordinated cations, M_i^{n+} is the proportion of network modifying cations, "i", with electrical charge $n+$ after subtraction of the portion required for charge-balancing trivalent cations on tetravalent sites (Mysen and Richet, 2005). The variation of Rc with NBO/T is reported in Fig. 9, along with the sigmoidal function that best fits our experimental data. The variation of Rc (°C/h) with our sub-alkaline silicate liquids joins the equation:

$$Log \; Rc = a \; /\{1+e^{-[(NBO/T-b)/c]} \} \qquad (2)$$

where a, b and c are fitting parameters equal to 3.814, 0.139 and 0.032, respectively. This equation reproduces data with a standard error of estimate of 0.18, but compositions close to R_{100} have low reproducibility (Fig. 9). The evolution of Rc with NBO/T indicates that B_{100} and $B_{80}R_{20}$ have similar GFA behaviours that rapidly change when liquid composition shifts from $B_{80}R_{20}$ to $B_{20}R_{80}$. It is possible that a further significant decrease of Rc occurs between $B_{20}R_{80}$ and R_{100}. However, the critical cooling rate of this latter liquid is overestimated (Fig. 5) since a defined trend of crystallization is not available and could be obtained only at cooling rates < 1 °C/h (see before).

The dependence of Rc with network modifier and network forming cations is in general agreement with previous experimental data, mainly summarised by studies of Uhlmann et al. (1981) and Fang et al. (1983). These authors reported 24 different (lunar) silicate liquids with SiO_2, Fe_2O_3 and Na_2O amounts of 36.6 - 58.7 wt.% (only two have SiO_2 > 50 wt.%), 6.7 - 23.5 wt.% and < 1 wt.%, respectively, for whom Rc values were defined by crystal contents of 1 vol.%. They measured the crystal content by X-ray diffraction or optical microscopy and not by BS-SEM analyses, that represents the unique method to fully observe textures in size ranges from sub-micrometric to millimetric scales. Unfortunately, Fang et al. (1983) and Uhlmann et al. (1981) did not reported textures of crystalline phases and fO_2 of experiments; importantly, the most part of their silicate liquids do not fully matches with our melt compositions, except four liquids with Rc of 10800 °C/h (sample 15086), 9720 °C/h (samples 15422 and 15301) and 7200 °C/h (sample15286 intrusion) These liquids have Rc and SiO_2 contents of the same order of those of B_{100} and $B_{80}R_{20}$,

whereas the other chemical components are significantly different. Intriguingly, the highest Rc values (14400 - 18000 °C/h) were measured for liquids with 36.6 wt.% < SiO_2 < 47.8 wt.% and 21.9 wt.% < Fe_2O_3 < 23.5 wt.%, in agreement with the trend of our data (Figs. 5 and 9). A silicate melt with a slight more alkaline character than $B_{60}R_{40}$ was investigated by Iezzi et al. (2011) under atmospheric conditions; they inferred Rc of 2200 °C/h, that is of the same order of 3020 °C/h measured for $B_{60}R_{40}$ (Fig. 5).

In volcanic rocks, critical cooling rates > 1000 °C/h are required to form glassy rocks with composition close to B_{100} and $B_{80}R_{20}$ (Table 1), as inferred on basaltic lavas and pumices cooled under subaerial and submarine environments (Cashman, 1993; Lesher et al., 1999; Szramek et al., 2010); Lesher et al., (1999) corroborated their inferences on the solidification regimes of tholeiitic basalts from the Tertiary North Atlantic ridge by dynamic experimental investigations aimed to reproduce these natural rock textures. Finally, the external portions of tholeiitic pillows from the Juan the Fuca Ridge (Zhou et al., 2000) show textural features very similar to those observed in our B_{100} run-products cooled at the highest rates; this latter study suggests that spinel is the first phase to crystallize, with a shape similar to those observed here; natural and rapidly formed spinels became larger and richer in Ti from the rims of pillows towards their interiors.

All these comparisons validate the evolution of GFA as a function of melt composition attained from our experiments (Fig. 9) and depicted by equation (2). Evolution trends of more alkaline liquid (Fig. 1) should be investigated to decipher the effect of each chemical species on the solidification behaviour.

5.2 *Reduced glass transition Trg.*

The reduced glass transition parameter, *Trg,* calculated for our six bulk liquids is reported in Table 1. Following the procedure reported in Iezzi et al. (2009), the melting temperature, *Tm,* was derived with MELTS (Ghiorso and Sack, 1995; Asimov and Ghiorso, 1998), whereas the glass transition, *Tg,* was obtained using viscosity models from literature (i.e., models of Hui and Zhang, 2007 and

Giordano et al., 2006 showing nearly identical results) (Table 1). In Fig. 10, our results are plotted in comparison with those of Fan et al. (2007) that compiled Trg and Rc values for different classes of glass-forming liquids, i.e. network (oxide, fluoride, as well as semiconductor), metallic and molecular sub-groups. All glass-forming liquids follow roughly an inverse logarithmic evolution in the Trg vs Rc plot (Fig. 10). Since this plot can not quantitatively describe the solidification behaviour of network, metallic and molecular liquids, Fan et al. (2007) suggested a new criterion based on the fragility of liquids to quantify the relationship between Trg and Rc. Gu et al. (2012) pointed out that a further new criterion based on Tx (the onset temperature of crystallization) is necessary to successfully reproduce the GFA of glass-forming liquids. However, Tx of natural silicate liquids have been measured only for a few SiO_2-poor melts (Ray et al., 2010; Applegarth et al., 2013).

Whatever the reasons for the limited reproducibility of GFA for glass-forming liquids, we can compare our bulk compositions with network forming systems; Fan et al. (2007) tabulated network liquids with a very different structural arrangement (SRO: short range order) such as simple silicate and/or aluminosilicate melts together with oxygen-free melts; this probably is responsible for the low quantitative correlation between Trg and Rc of network glass-forming liquids reported by Fan et al. (2007) (Fig. 10). On the other hand, our sub-alkaline silicate melts follow a well defined trend (Fig. 10), according to the following power equation:

$$Rc = a * Trg^{-b} \qquad (3)$$

where a and b are $1.19*10^{-4}$ and -28.7, respectively ($R^2 = 0.92$). The good reproducibility of our data by this simple power equation probably relies on the similarity of SRO for our silicate liquids and to their relative low fragility changes compared to other network liquids (Fig. 10). In fact, fragility, F, is a measure of the deviation from Arrhenian behaviour in a plot relating viscosity and temperature (Angell, 1995; Debenedetti and Stillinger, 2001; Giordano and Dingwell, 2003). Taking in account that the fragility of a silicate liquid is related to NBO/T (Giordano and Dingwell, 2003), then it results that Rc can be correlated with F as well; hence, F increases from R_{100} to B_{100}

(Table 1). In addition to the variation of *Trg* as a function of NBO/T, we observe that as *F* increases from R_{100} to B_{100}, this corresponds to an increased facility to nucleate crystals and, *viceversa*, an increased difficulty to glassify (Table 1).

5.3 Effects of sample containers and micro-bubbles.

At low *f*O_2, the marked effect of Pt on nucleation of SiO_2-poor, FeO-rich melts has been well established since long time (Berkebile and Dowty, 1982). In our highly oxidized experiments, sp preferentially nucleate on Pt only a few microns next to the capsule wall and sp crystals are equally distributed in its proximity or far into the melt. Consequently, it can be excluded that Pt substrata control the whole solidification behaviour of run-products (Figs. 4 and Table 3). This is in agreement with previous kinetic solidification experiments showing as SiO_2-poor melts can be affected by a weak heterogeneous nucleation on Pt only at high buffering conditions (Iezzi et al., 2008 and 2011; Mollo et al., 2012b).

The amount of H_2O < 400 ppm (Table 1), after a protracted superheated treatment of the E0 run-products (Table 2 and Fig. 2), determines a very low amount of micro-metric bubbles (<< 1 area%) at the onset of temperature decrease. We do not observe appreciable preferential crystallization of crystals on these micrometric bubbles, in agreement with observations reported in Vetere et al. (2013). Therefore, the solidification behaviour observed in this study can be entirely attributed to the intrinsic behaviour of the investigated melts (Table 1).

5.4 Crystallization sequence.

At high degrees of crystallization it is difficult to establish the order of appearance of minerals, but run-products with a low crystal content show that sp is the first phase on liquidus in each starting melt (Figs. 4, 5 and 6). This is clearly evidenced by the radial distribution of cpx around sp crystals (Figs. 4a and 4b and 11). The rapid appearance of sp in B_{100} - R_{100} liquids is also suggested by the lack of sp-free run-products with low crystal contents. At the same time, run-

products with cpx content of about 2 area% are obtained at cooling rates slightly lower than those used to derive Rc (Figs. 5 and 6). These features are straightforward evidenced by run-products $B_{60}R_{40}$ at 1800-180 °C/h, $B_{40}R_{60}$ at 180-60 °C/h and $B_{20}R_{80}$ at 7, 60 and 180 °C/h, able to crystallise cpx only when they contain comparable amounts of sp, whereas abundant cpx crystallization is observed at much lower cooling rate conditions (see discussion above and Fig. 6). For B_{100} and $B_{80}R_{20}$ run-products, this effect is less apparent since the amount of cpx suddenly increases from 9000 to 1800 °C/h (Fig. 6). As showed in Fig. 11, cpx nucleates and grows by far only around sp crystals, demonstrating that its crystallisation is due to heterogeneous nucleation on sp (see below). Therefore, at high cooling kinetics, sp more easily nucleates with respect to silicate minerals, whereas cpx readily crystallizes on sp rather than from the melt (Figs. 6 and 11). A high degree of cpx crystallization occurs only between 9000-1800, 1800-180, 180-60 and 7-1 °C/h for B_{100}, $B_{80}R_{20}$, $B_{60}R_{40}$, $B_{40}R_{60}$ and $B_{20}R_{80}$, respectively.

As the liquid composition shifts from B_{100} to $B_{20}R_{80}$, cpx starts to crystallise on sp at fast kinetic conditions, but its abundance is very low; conversely, cpx crystallises markedly at lower cooling rates as a function of the melt composition that is close to that of the starting melt due to the low crystallization of sp (Fig. 6). This behaviour is showed in Fig. 12, where NBO/T (or bulk composition) is plotted *vs* cooling rate and *vs* crystal content. The most mafic compositions (B_{100} and $B_{20}R_{80}$) show important variations in the crystal content (mainly cpx), whereas the degree of crystallization decreases with decreasing NBO/T even at slow cooling rates.

5.5 Heterogeneous nucleation.

For each bulk composition, the above observations imply that cpx crystallises only around sp at high kinetic conditions (Fig. 11) whereas, at lower cooling rates, cpx solidifies throughout the whole silicate liquid. The heterogeneous crystallisation of cpx on sp allows a fast appearance relative to direct precipitation from the melt. This effect can produce only a limited amount of crystalline phases; conversely, the abundant crystallisation of cpx is mostly controlled by the

intrinsic physico-chemical properties of residual liquid(s), i.e., as NBO/T decreases of from B_{100} to $B_{20}R_{80}$ (Figs. 6 and 12).

A similar situation is observed for plg at 60-7 °C/h for $B_{80}R_{20}$ and 1-7 °C/h for $B_{40}R_{60}$, where plg occurs prevalently on cpx rims (see Figs. 4, 6, and 11). The heterogeneous nucleation of cpx on sp and plg on cpx seems to shorten the time of appearance, but most of the crystallisation (> 5, 10, 20, 30, 40 and 50 area%) of cpx and/or plg remains controlled by the physical-chemical features of the liquid and thus by the chemical diffusivity in residual melts (Fig. 12).

Heterogeneous nucleation reduces the energy required to form a crystal on a pre-existing surface in comparison to homogeneous nucleation; the energy required for the heterogeneous crystallization is progressively reduced as the similarity of atomic structures between pre-existing and new forming nuclei increases (Lofgren, 1983; Lasaga, 1997; Mollo et al., 2012b). However, these crystalline structural similarities limit the concentrations of chemical feeding elements in the silicate liquid surrounding the new growing crystals; in turn, this process is halted or new crystals start to grow perpendicularly to the heterogeneous nucleation surface (Higgins, 2006; Mollo et al., 2012b). This explains the radial distribution of elongated tiny cpx crystals around early-formed sp phases and their low amounts at high cooling conditions (Figs. 4a, 4b, 5, 6 and 11). At moderate to high crystal contents, cpx and plg also appear disposed along defined linear directions (Figs. 4a and 4b and 11); this suggests crystal growth over the effect of crystallographic directions and perhaps heterogeneous crystallization mechanisms (Hammer et al., 2010; Walter et al., 2013). Finally, an intriguing feature is provided by BSE microphotographs acquired at very high magnification (Fig. 4c) giving the possibility to appreciate sp crystals at the sub-micrometric scale. Many of these sp host in their central portions "very bright and sub-micrometric blebs" that can be interpreted as Fe-rich phases.

5.6 Metastable nucleation and complex crystallization trends.

As NBO/T and Fe (Mg and Ca) decrease and Si (Na, K and to a lesser extent Al) increases in the liquids (Table 1), the first crystalline phase occurs at progressively lower cooling rates (Figs. 5, 6 and 9). As documented above, sp crystallises as liquidus phase followed by cpx, whereas plg forms only at moderate to low cooling rates. This crystallization sequence agrees with the nucleation theory; under dynamic conditions, crystalline phases with lower energetic barriers of formation are more favoured to nucleate (Kirkpatrick 1983; Lasaga 1997; Zhang 2008; Iezzi et al. 2008, 2009, 2011). Nucleation requires random compositional fluctuations of molecular units in the melt below the liquidus temperature; stable nuclei can form only when the local arrangement of molecular units attains a critical dimension (Lasaga, 1997; Zhang 2008). Compositional fluctuations are probabilistic in nature and involve the breaking and formation of chemical bonds; consequently strong chemical bonds (network-forming cations) can explore a more limited compositional space, i.e. the compositional difference between the initial liquid and the final structural arrangement (Roskosz et al. 2006a, 2006b; Iezzi et al., 2014). The opposite occurs for chemical elements that rapidly diffuse in the melt (network-modifier cations). Thereby, the energetic barrier of nucleation scales with the number and strength of chemical bonds; in our compositional systems, the most strong and abundant bonds are ^{IV}Si-O, followed by ^{IV}Al-O and $^{IV}Fe^{3+}$-O (Kirkpatrick 1983; Dingwell 2006; Iezzi et al. 2008, 2009, 2011; 2014). This explains the quick and early nucleation of sp, followed by the crystallization of cpx and plg (this latter at low cooling conditions; Figs. 5 and 6).

The complex relationship between texture and composition of glass and minerals is well explained by the complex and apparently scattered crystal content of $B_{80}R_{20}$ run-product as a function of cooling rate (Fig. 5). As the cooling rate increases from 1 to 180 °C/h, the crystal content first decreases abruptly and then slightly increases (Fig. 5); indeed, the amount of cpx continuously increases, but plg is abundant only in run-products containing cpx content < 25 area% (Table 3 and Fig. 6). The increasing cpx content is accompanied by incorporation of higher Al_2O_3 concentrations in the crystal lattice (Fig. 8), implying that the residual melt is progressively more

reluctant to crystallise plg (Tables 1 and 4); moreover, as the cooling rate increases plg is forced to crystallise with a more anorthitic character, i.e. Al- and Ca-rich crystals (Mollo et al., 2011; Iezzi et al., 2008; 2011; 2014). These mechanisms causes that the residual melt is depleted in Al (and enriched in Si) hampering the nucleation of significant amounts of (anorthite-rich) plg. The same explanation holds for the abundant formation of plg at 1 and 7 °C/h for $B_{60}R_{40}$; at these two rates the amount of cpx is ≤ 21.5 area% and plg is more favoured to nucleate (Fig. 6).

Similar competing mechanisms between the amount and composition of early formed phases and chemical element enrichments and depletions in the residual melts can be invoked to explain almost constant crystalline trends observed at different cooling rates (Figs. 5 and 6). Notably, the B_{100} run-products at 1, 7 and 60 have crystal contents of about 100 area% and at 180 and 1800 °C/h have about 40 area% of crystals (Table 3 and Fig. 5); the variable kinetic conditions during melt solidification can be actually revealed only by means of cpx composition, abundance, aspect ratio and size dimension (Figs. 4a, 4b, 6 and 8). A similar situation holds for the $B_{40}R_{60}$ run-products at 1, 7 and 60 °C/h (Figs. 4a, 4b, 6 and 8).

5.7 Volcanological implications.

The dynamic cooling experiments presented in this study represent an oversimplification of natural processes taking place over the effect of variable fO$_2$ values, volatile species dissolved in the melt, bubble and/or crystal contents, cooling and decompression rates, and latent heats of crystallisation. However, magma en route to the Earth surface becomes progressively oxidised (Burgisser and Scaillet, 2007) and can be also re-heated (Blundy et al., 2006), thus enhancing the loss of volatiles and re-melting of crystals. Therefore, results presented here have to be considered with caution when applied to strictly reconstruct natural solidification conditions. Owing these limitations, the evolution of textures from our cooling rate experiments can aid to semi-quantitative elucidate cooling of magmas on Earth (lavas, pumices, bombs) and perhaps on other planets and meteorites. In parallel, the intrinsic solidification behaviour of natural silicate liquids (i.e., in

absence of heterogeneous surfaces at the beginning of cooling, Figs. 5, 6, 7, 8 and 9) can be used to discriminate the crystallization path of magmas from the Earth interior to the surface.

On the Earth surface, cooling rates span a huge range of magnitudes mainly as a function of the volume of erupted magmatic products and the distance from the cold to the hot portions. Silicate liquids mainly cool by conductive and radiative heat transfer (Neri, 1998; Xu and Xhang, 2002; Harris et al., 2005; Whittington et al., 2009). Rates on the order of 10^5 (9000) - 10^2 (> 180) °C/h occur during the cooling of mm- to few cm-thick silicate liquids (Zhou et al., 2000; Xu and Zhang, 2002); hence, run-products in this regime (Table 3) can be used to constrain the solidification of lavas at the contact with air or seawater, and/or the solidification of bombs and pyroclastic ashes. Rates ≤ 180 °C/h instead can be attained by lava flows with thickness of the order of meters.

To gain insights on the significance of our experiments for natural cooling conditions, we used 2-D numerical simulations based on an explicit finite-difference scheme (cf. Wohletz et al., 1999 and references therein); these simulations account for conductive cooling of two virtual B_{100} and R_{100} lavas with variable thickness, cooled from 1300 °C down to the temperature of air and soil assumed to be 25 °C; physico-chemical parameters used in our simulations are summarised in Table 6. It is important to note that, in lavas, heat dissipation can also increases by radiation and heat transfer due to fractures and/or gas release. Thus, we consider our simulations as conservative with respect to those occurring under natural conditions. Our computations focus on the cooling rates obtained in response to the silicate thicknesses; obviously, B_{100} cools slower than R_{100} due to its lower thermal diffusivity (Table 6). Results from these simulations are reported in Figs. 13a and 13b as a function of temperature, time and distance from the lava-air interface. Our simulated lavas have thickness of 0.5, 1, 2, 3, 5 and 10 m and compositions corresponding to B_{100}. The positions inside lavas corresponding to the investigated cooling rates (Table 2 and Fig. 2).

With increasing lava thickness, the cooling rate shifts towards the outermost regions (Figs. 13a and 13b); cooling rates of 1800 and 180°C/h occur only in the uppermost lava portions (Figs. 13a and 13b). A cooling rate of 60 °C/h operates only at 0.1-0.2 m from the uppermost lava surface.

The temperature of 0.5-metre-thick lava decreases to 800 °C in its core after 30-40 hours, when the cooling rate is comprised between 60 and 7 °C/h (Fig. 13a). A cooling rate of 7 °C/h is measured at 0.1 m from the uppermost and lowermost portions of 1-metre-thick lava, whereas the temperature of the lava core decreases to 800 °C after about 100 hours over the effect of a cooling rate between 7 and 1 °C/h (Fig. 13a). A rate of 1 °C/h is able to simulate the cooling conditions operating in the middle portion of 2-metre-thick lavas (Fig. 13a); otherwise, this cooling rate reproduces the cooling conditions operating 1 meter below the uppermost surfaces of 3-, 5- and 10-metre-thick lavas (Fig. 13b).

By comparing Figs. 5, 6 and 13 we can provide possible textures and crystalline assemblages encountered in aphyric, nearly anhydrous lavas. Nonetheless, as discussed above, heterogeneous nucleation effects (due to a limited number of sp crystals) should not significantly increase the crystal content, since a marked increase of crystals should be due to the chemical composition of the molten fraction. It then follows that our experimental results (Figs. 4, 5, 6, 7, 8 and 9) together with numerical simulations (Figs. 13a and 13b) can be also applicable to lavas erupted with crystals (and possibly bubbles). In this context, cooling rate and crystallization can be considered as the main parameters causing changes in the rheological properties of lavas (Robert et al., 2014 and reference therein). Therefore, results displayed in Figs. 5, 6 and 13 can help to constrain the temperature-time-viscosity paths of flowing lavas (Table 1). R_{100} and $B_{20}R_{80}$ are unable to crystallise in lavas with thickness < 1 and 0.5 m, whereas other compositions can easily crystallise from thickness even lower than 0.5 m (Figs. 5, 13a and 13b). Noteworthy, the complex crystallization trends described in Fig. 5 as a function of cooling rate suggest that the crystal content do not necessarily increases from the outermost towards innermost portions of lavas.

A final aspect is that, from outermost to innermost portions of lavas and from B_{100} to R_{100} liquid compositions, it is more difficult to discriminate minerals formed by cooling under sub-aerial (or sub-marine) conditions, and those formed before eruption. As a result, solidification conditions of lavas developed before their eruptions are more preserved in their outermost portions (in the

absence of sinking of crystals), especially for SiO_2-poor liquids. Crystals with sizes up to 1 mm form over the effect of a simple linear cooling. Therefore, large microphenocrysts and phenocrysts cannot be unequivocally indicative of growth before eruptions (cf. Lanzafame et al., 2013).

6. CONCLUSIONS

The suppression of crystallization in our sub-alkaline silicate liquids occurs at cooling rates between 1 to 9000 °C/h; Rc correlates with NBO/T parameter and decreases from basalt to rhyolite. The correlation between bulk composition and crystal content well explains the common occurrence of obsidians with rhyolitic to dacitic compositions and the scarce presence of glass-rich (> 50 area%) volcanic rocks with a basaltic composition (Figs. 4, 5, 6, 9 and 12). The fact that a significant amount of crystals (up to 100 area%) with large sizes (up to 1 mm) form over the effect of cooling rate indicates that cautions should be taken for the interpretation of volcanic rock textures.

The crystallization path of a natural silicate melt can be extremely complex; generally, with decreasing cooling rate, the crystal content increases but it can be that the crystal content remains constant or even decreases (Fig. 5). The amount and composition of early-formed crystalline phases determine the chemical composition of residual melts from which late phases can (or not) crystallize (Figs. 6, 7 and 8). Cpx forms over the effect of high cooling rate conditions being enriched in Al; consequently, the residual melt becomes progressively enriched in Si and reluctant to nucleate.

Sp determines the GFA behaviour of sub-alkaline silicate liquids at ambient conditions (Figs. 5 and 6); this implies that the initial content of Fe and its speciation imposed by fO_2 can eventually control the onset of nucleation and Rc. However, sp is responsible for the formation of a few area% of crystals, whereas abundant crystallisation of minerals with silicate-based structures (cpx and plg) is due the short range order of residual molten fractions (Fig. 12). Heterogeneous

nucleation effects on early formed sp are able to reduce the appearance of cpx, but they are unable to induce a significant increase of silicate crystals.

Glass-ceramic and ceramic materials are produced and used worldwide for many different purposes (Mauro and Zanotto, 2014). Sub-alkaline silicate liquids with natural and complex compositions follow the same general behaviour of synthetic network glass-forming liquids with relative simple compositions. The range of critical cooling rates of sub-alkaline liquids (Figs. 9 and 10) and their GFA properties overlap in part with that of many network glasses used for technical and industrial applications (Fig. 10). Considering the huge abundance of natural rocks with compositions similar to those investigated here, it is then possible to design new, inexpensive ceramic materials, either glassy or with a desired crystal-content, by modulating the cooling rate and melt composition.

References

Applergarth, L.J., Tuffen H., James, , M.R. Pinkerton, H., 2013. Degassing-driven crystallisation in basalts. Earth-Science Reviews, 116, 1-16.

Angell, C.A., 1995. Formation of glasses from liquids and biopolymers. Science, 267, 1924-1935.

Armienti, P., 2008. Decryption of igneous rock textures: crystal size distribution tools, in: Putirka, K.D., Tepley, F.J. (Eds.). Reviews in Mineralogy, 69, 623-649.

Armienti, P., Pareschi, M.T., Innocenti, F., Pompilio, M., 1994. Effect of magma storage on the kinetics of crystals growth. Contribution to Mineralogy and Petrology, 115, 402-414.

Asimow, P.D., Ghiorso, M.S., 1998. Algorithmic modifications extending MELTS to calculate subsolidus phase relations. American Mineralogist 83, 1127-1131.

Avramov, I., Zanotto, E.D., Prado, M.O., 2003. Glass-forming ability versus stability of silicate glasses. II. Theoretical demonstration. Journal of Non-Crystalline Solids, 320: 9-20.

Baker, M.B., Grove, T.L., 1985. Kinetic controls on pyroxene nucleation and metastable liquid lines of descent in a basaltic andesite. American Mineralogist 70, 279-287.

Berkebile, C.A., Dowty, E., 1982. Nucleation in laboratory charges of basaltic composition. American Mineralogist 67, 886-899.

Bianco A. S. and Taylor L. A., 1977. Applications of dynamic crystallization studies: lunar olivine normative basalts. Proceeding of Lunar Science Conference, 8, 1593-1610.

Blundy, J., Cashman, K.V., Humphreys, M.C.S., 2006. Magma heating by decompression-driven crystallisation beneath andesite volcanoes. Nature, 443, 76-80.

Burgisser, A., Scaillet, B., 2007. Redox evolution of a degassing magma rising to the surface. Nature 445, 194-197.

Burkhard, D.J.M., 2005. Nucleation and growth rates of pyroxene, plagioclase, and Fe-Ti oxides in basalt under atmospheric conditions. European Journal of Mineralogy 17, 675-685.

Cabral, A.A., Cardoso, A.A.D., Zanotto, E.D., 2003. Glass-forming ability versus stability of silicate glasses. I. Experimental test. Journal of Non-Crystalline Solids, 320, 1-8.

Cashman, K.V., 1989. Relationship between plagioclase crystallization and cooling rate in basaltic melts Contributions to Mineralogy and Petrology, 113, 126-142

Cashman, K.V., 1991. Textural constraints on the kinetics of crystallization of igneous rocks, in: Nicholls, J., Russell, J.K. (Eds.). Reviews in Mineralogy, 24, 259-309.

Cashman, V., 1993. Relationship between plagioclase crystallization and cooling rate in basaltic melts. Contributions to Mineralogy and Petrology, 113, 126-142.

Conte, A., Perinelli, C., Trigila, R., 2006. Cooling kinetics experiments on different Stromboli lavas: effects on crystal morphologies and phase composition. Journal of Volcanology and Geothermal Research, 155, 179-200.

Corrigan, G.M., 1982. Supercooling and the crystallization of plagioclase, olivine, and clinopyroxene from basaltic magmas. Mineralogical Magazine, 46, 31-42.

Debenedetti, P.G., Stillinger, F.H., 2001. Supercooled liquids and the glass transition. Nature, 410, 259-267.

Del Gaudio, P., Mollo, S., Ventura, G., Iezzi, G., Taddeucci, J., Cavallo, A., 2010. Cooling rate-induced differentiation in anhydrous and hydrous basalts at 500 MPa: implications for the storage and transport of magmas in dikes. Chemical Geology, 270, 164-178.

Dingwell, D.B., 2006. Transport properties of magmas: diffusion and rheology. Elements, 2, 281-286.

Dowty, E., 1980. Crystal growth and nucleation theory and the numerical simulation of igneous crystallization, in: Hargraves, R.B. (Ed.), The physics of magmatic processes. Princeton University Press, New York, pp. 419-485.

Donaldson, C.H., 1979. An experimental investigation of the delay in nucleation of olivine in mafic magmas. Contribution to Mineralogy and Petrology, 69, 21-32

Dunbar, N.W., Riciputi, L.R., Jacobs, G.K., Naney, M.T., Christie, W., 1993. Generation of rhyolitic melt in an artificial magama: implications for fractional crystallization processes in natural magmas. Journal of Volcanology and Geothermal Research, 57, 157-166.

Dunbar, N.W., Jacobs, G.K., Naney, M.T., 1995. Crystallization processes in an artificial magma: variations in crystal shape, growth rate and composition with melt cooling history. Contribution to Mineralogy and Petrology, 120, 412-425.

Fan, G.J., Choo, H., Liaw, P.K., 2005. Fragility of metallic glass-forming liquidus: a simple thermodynamic connection. Journal of Non-Crystalline Solids, 351, 3879-3883.

Fan, G.J., Choo, H., Liaw, P.K., 2007. A new criterion for the glass-forming ability of liquidus. Journal of Non-Crystalline Solids, 353, 102-107.

Fang, C.Y., Yinnon H., Uhlmann, D.R., 1983. Cooling rates for glass containing lunar compositions. Proceedings of the 13th lunar and planetary science conference, part 2. Journal of Geophysical research, 88: A907-A911.

Faure, F., Trolliard, G., Nicollet, C., Montel, J.M., 2003. A development model of olivine morphology as a function of the cooling rate and the degree of undercooling. Contribution to Mineralogy and Petrology, 145, 251-263.

Faure, F., Schiano, P., Trolliard, G., Nicollet, C., Soulestin, B., 2007. Textural evolution of polyhedral olivine experiencing rapid cooling rates. Contribution to Mineralogy and Petrology, 153, 405-416.

Fenn, P.M., 1977. The nucleation and growth of alkali feldspars from hydrous melts. Canadian Mineralogist, 15, 135-161.

Ghiorso, M.S., Sack, R.O., 1995. Chemical mass-transfer in magmatic processes 4. A revised and internally consistent thermodynamic model for the interpolation and extrapolation of liquidus-solid equilibria in magmatic systems at elevated temperatures and pressures. Contribution to Mineralogy and Petrology, 119, 197-212.

Gibb, F.G.F., 1974. Supercooling and crystallization of plagioclase from a basaltic magma. Mineralogical Magazine, 39, 641-653.

Giordano, D., Dingwell, D.B., 2003. The kinetic fragility of natural silicate melts. Journal of Physics and Condensed Matter 15, 945-954.

Giordano, D., Mangiacapra, A., Potuzak, M., Russel, J.K., Romano, C., Dingwell, D.B., Di Muro, A., 2006. An expanded non-Arrhenian model for silicate melt viscosity: a treatment for metaluminous, peraluminos and peralkaline liquids. Chemical Geology, 229, 42-56.

Grove, T.L., and Raudsepp, M., 1978. Effects of kinetics on the crystallization of quartz normative basalt 15597: an experimental study. Proceeding of Lunar Science Conference, 9, 585-599.

Gu, B., Liu, F., Jiang, Y., Zhang, K., 2012. Evaluation of glass-forming ability criterion from phase-transformation kinetics. Jounral of Non-Crystalline Solids, 358, 1764-1771.

Guo, S., Lu, Z.P., Liu, C.T., 2010. Identify the best glass forming ability criterion. Intermetallics, 18, 883-888.

Hammer, J.E., 2008. Experimental studies of the kinetics and energetics of magma crystallization, in: Putirka, K.D., Tepley, F.J. (Eds.). Reviews in Mineralogy, 69, 9-59.

Hammer, J.E., 2009. Application of a textural geospeedometer to the late-stage magmatic history of MIL 03346. Meteoritics & Planetary Science, 44, 141-154.

Hammer, J.E., Sharp, T.G., Wessel, P., 2010. Heterogeneous nucleation and epitaxial crystal growth of magmatic minerals. Geology, 38, 367-370.

Harris, A.J.L., Bailey, J., Calvari, S., Dehn, J., 2005. Heat loss measured at a lava channel and its implications for down-channel cooling and rheology, in: Manga, M., Ventura, G. (Eds.), Kinematics and dynamics of lava flows of lava flows. Geological Society of America, Boulder, Special Paper, 396, 125-146.

Higgins, M.D., 2000. Measurement of crystal size distributions. American Mineralogist, 85, 1105-1116.

Higgins, M.D., 2006. Quantitative Textural Measurements in Igneous and Metamorphic Petrology. Cambridge University Press, Cambridge.

Hui, H., Zhang, Y., 2007. Toward a general viscosity equation for natural anhydrous and hydrous silicate melts. Geochimica et Cosmochimica Acta, 71, 403-416.

Iezzi, G., Mollo, S., Ventura, G., Cavallo, A., Romano, C., 2008. Experimental solidification of anhydrous latitic and trachytic melts at different cooling rates: the role of nucleation kinetics. Chemical Geology, 253, 91-101.

Iezzi, G., Mollo, S., Ventura, G., 2009. Solidification behaviour of natural silicate melts and volcanological implications, in: Lewis, N., Moretti, A. (Eds.), Volcanoes: Formation, Eruptions and Modelling. Nova publishers, New York, 127-151.

Iezzi, G., Mollo, S., Torresi, G., Ventura, G., Cavallo, A., Scarlato, P., 2011. Experimental solidification of an andesitic melt by cooling. Chemical Geology, 283, 261-273.

Iezzi, G., Mollo, S., Shahini, E., Cavallo, A., Scarlato, P., 2014. The cooling kinetics of plagioclase feldspars as revealed by electron-microprobe mapping. American Mineralogist, 99, 898-907.

Kirkpatrick, R.J., 1981. Kinetics of crystallization of igneous rocks, in: Lasaga, A.C., Kirckpatrick, R.J. (Eds.). Reviews in Mineralogy and Geochemistry, 8, 321-397.

Kirkpatrick, R.J., 1983. Theory of nucleation in silicate melts. American Mineralogist, 68, 66-77.

Kirkpatrick, R.J., Kuo, L.C., Melchior, J., 1981. Crystal growth in incongruently-melting compositions: programmed cooling experiments with diopside. American Mineralogist, 66, 223-241.

Kirkpatrick, R.J., Reck, B.H., Pelly, I.Z., Kuo, L.C., 1983. Programmed cooling experiments in the system MgO-SiO2: kinetics of a peritectic reaction. American Mineralogist, 68, 1095-1101.

Klöß, G.H., 2000. Dichtefluktuationen natürlicher Gläser. (Dissertation) University of Jena.

Lanzafame, G., Mollo, S., Iezzi, G., Ferlito, C., Ventura, G., 2013. Unraveling the solidification path of a pahoehoe "cicirara" lava from Mount Etna volcano Bulletin of Volcanology 75, 703, DOI 10.1007/s00445-013-0703-8.

Lasaga, A.C., 1997. Kinetic Theory in the Earth Sciences. Princeton University Press, Princeton, New York.

Lesher, C.E., Cashman, K.V., and Mayfield, J.D., 1999. Kinetic controls on crystallization of Tertiary North Atlantic basalt and implications for the emplacement and cooling history of lava at Site 989, Southeast Greenland rifted margin, in: Larsen, H.C., Duncan, R.A., Allan, J.F., and Brooks, K. (Eds.). Proceeding of the ODP Scientific results, 163, 135-148.

Lofgren, G. E., 1977. Dynamic crystallization experiments bearing on the origin of textures in impact generated liquids. Proceeding of Lunar Science Conference, 8, 2079-2095.

Lofgren, G., 1980. Experimental Studies on the Dynamic Crystallisation of Silicate Melts, in: Hargraves, R.B. (Ed.), The physics of magmatic processes. Princeton University Press, New York, pp. 487-551.

Lofgren, G. E., 1983. Effect of heterogeneous nucleation on basaltic textures: A dynamic crystallization study. Journal of Petrology, 24, 229-255.

Lofgren, G. E., 1989. Dynamic crystallization of chondrule melts of porphyritic olivine omposition: textures experimental and natural. Geochimica et Cosmochimica Acta, 53, 461-470.

Lofgren G., Donaldson C. H., Williams R. J., Mullins O., Jr. and Usselman M., 1974. Experimentally reproduced textures and minerals chemistry of Apollo 15 quartz normative basalts. Proceeding of Lunar Science Conference, 5, 549-567.

Lofgren, G. E., Grove, T. L., Brown, R. W., Smith, D. P., 1979. Comparison of dynamic crystallization techniques on Apollo 15 quartz normative basalts. Proceeding of Lunar Science Conference, 10: 423-438.

Lofgren, G., Russell, W.J., 1986. Dynamic crystallization of chondrule melts of porphyritic and radial pyroxene composition. Geochimica et Cosmochimca Acta, 50, 1715-1726.

Lu, Z.P., Li, Y., Ng, S.C., 2000. Reduced glass transition temperature and glass forming ability of bulk glass forming alloys. Journal of Non-Crystalline Solids, 270, 103-114.

Mauro, J.C., Zanotto, E.D., 2014. Two Centuries of Glass Research: Historical Trends, Current Status, and Grand Challenges for the Future. International Journal of Applied Glass Science, 5, 313-327.

Mollo, S., Del Gaudio, P., Ventura, G., Iezzi, G., Scarlato, P., 2010. Dependence of clinopyroxene composition on cooling rate in basaltic magmas: implications for thermobarometry. Lithos, 118, 302-312.

Mollo, S., Putirka, K., Iezzi, G., Del Gaudio, P., Scarlato, P., 2011. Plagioclase-melt disequilibrium due to cooling dynamics: implications for thermometry, barometry and hygrometry. Lithos, 125, 221-235.

Mollo, S., Misiti, V., Scarlato, P., Soligo, M., 2012a. The role of cooling rate in the origin of high temperature phases at the chilled margin of magmatic intrusions. Chemical Geology, 322-323, 28-46.

Mollo, S., Iezzi, G., Ventura, G., Cavallo, A., Scarlato, P., 2012b. Heterogeneous nucleation mechanisms and formation of metastable phase assemblages induced by different crystalline seeds. Journal of Non-Crystalline Solids, 358, 1624-1628.

Mondal, K., Murty, B.S., 2005. On the parameters to assess the glass forming ability of liquids. Journal of Non-Crystalline Solids, 351, 1366-1371.

Mysen, BO, Richet, P., 2005. Silicate Glasses and Melts, Properties and Structure. Elsevier, Amsterdam, 544 pp.

Nabelek P.I., Hofmeister, A.M., Whittington, A.G., 2012. The influence of temperature-dependent thermal diffusivity on the conductive cooling rates of plutons and temperature-time paths in contact aureoles. Earth and Planetary Science Letters, 317, 157-164.

Naney, M.T., Swanson, S.E., 1980. The effect of Fe and Mg on crystallization in granitic systems. American Mineralogist, 65, 639-653.

Neri, A., 1998. A local heat transfer analysis of lava cooling in the atmosphere: application to thermal diffusion-dominated lava flows. Journal of Volcanology and Geothermal Research, 81, 215-243.

Ni, H., Keppler, H., Walte, N., Schiavi, F., Chen, Y., Masotta, M., Li, Z., 2014. In situ observation of crystal growth in a basalt melt and the development of crystal size distribution in igneous rocks Contribution to Mineralogy and Petrology 167, 1003. DOI 10.1007/s00410-014-1003-9

Orlando, A., D'Orazio, M., Armienti, P., Borrini, D., 2008. Experimental determination of plagioclase and clinopyroxene crystal growth rates in an anhydrous trachybasalt from Mt Etna (Italy) European Journal of Mineralogy, 20, 653-664.

Pupier, E., Duchene, S., Toplis, M.J., 2007. Experimental quantification of plagioclase crystal size distribution during cooling of a basaltic liquid. Contribution to Mineralogy and Petrology, 155, 555-570.

Ray, C.S., Reis, S.T., Brow, R.K., Höland, W., Rheinberger V., 2005. A new DTA method for measuring critical cooling rate for glass formation. Journal of Non-Crystalline Solids, 351, 1350-1358.

Ray, C.S., Reis, S.T., Sen, S., O'Dell, J.S., 2010. JSC-1A lunar soil simulant: Characterization, glass formation, and selected glass properties. Journal of Non-Crystalline Solids, 356: 2369-2374.

Romine, W.L., Whittington, A.G., Nabelek, P.I., Hofmeister, A.M., 2012. Thermal diffusivity of rhyolitic glasses and melts: effects of temperature, crystals and dissolved water. Bulletin of Volcanology, 74, 2273-2287.

Roskosz, M., Toplis, M.J., and Richet, P., 2006a. Kinetic vs. thermodynamic control of nucleation and growth in molten silicates. Journal of Non-Crystal Solids, 352, 180-184.

Roskosz, M., Toplis, M.J., and Richet, P., 2006b. Crystallization of highly supercooled silicate melts. Advanced Engineering Materials, 8, 1224-1228.

Schiavi, F., Walte, N., Konschak, A., Keppler, H., 2009. First in situ observation of crystallization processes in a basaltic-andesitic melt with the moissanite cell. Geology, 37, 963-966.

Shelby, J.E., 2005. Introduction to Glass Science and Technology, 2nd edition. Padstow, Conwall, UK.

Sharp, T.G., Stevenson, R.J., Dingwell, D.B., 1996. Microlites and "nanolites" in rhyolitic glass: microstructural and chemical characterisation. Bulletin of Volcanology, 57, 631-640.

Sparks, R.S.J., Murphy, M.D., Lejeune, A.M., Watts, R.B., Barclay, J., Young, S.R., 2000. Control on the emplacement of the andesite lava dome of the Soufriere Hills volcano, Montserrat by degassing-induced crystallization. Terra Nova, 12, 14-20.

Szramek, L., Gardner, J. E., Hort, M., 2010. Cooling-induced crystallization of microlite crystals in two basaltic pumice clasts. American Mineralogist, 95, 503-509.

Sunagawa, I., 1992. In situ investigation of nucleation, growth, and dissolution of silicate crystals at high temperatures. Annual Reviews of Earth and Planetary Science, 20, 113-142.

Swanson, S.E., 1977. Relation of nucleation and crystal-growth rate to the development of granitic textures. American Mineralogist, 62, 966-978.

Swanson, S.E., Naney, M.T.,Westrich, H.R., Eichelberger, J.C., 1989. Crystallization history of Obsidian Dome, Inyo Domes, California. Bulletin of Volcanology, 51, 161-176.

Tsuchiyama, A., 1983. Crystallization kinetics in the system CaMgSi2O6-CaAl2Si2O8: the delay in nucleation of diopside and anorthite. American Mineralogist, 68, 687-698.

Uhlmann, D.R., Onorato, P.I.K., and Scherer, G.W. (1979). A simplified model for glass formation. Proceeding of Lunar Science Conference, 10, 375-381.

Uhlmann, D.R., Yinnon, H., and Fang, C.-H. (1981). Simplified model evaluation of cooling rates for glass-containing lunar compositions. Proceeding of Lunar Science Conference, 12, 281-88.

Vetere, F., Iezzi, G., Behrens, H., Cavallo, A., Misiti, V., Dietrich, M., Knipping, J., Ventura, G., Mollo S., 2013. Intrinsic solidification behaviour of basaltic to rhyolitic melts: a cooling rate experimental study. Chemical Geology, 354, 233-242.

Vona, A., Romano, C., 2013. The effects of undercooling and deformation rates on the crystallization kinetics of Stromboli and Etna basalts. Contributions to Mineralogy and Petrology, 166, 491-509.

Walker, D., Kirkpatrick, R.J., Longhi, J. and Hays, J.F., 1976. Crystallization history of lunar picritic basalt sample 12002: phase-equilibria and cooling-rate studies. Geological Society of America Bulletin, 87, 646-656.

Walker, D., Powell, M.A., Lofgren, G.E., and Hays, J.F., 1978. Dynamic crystallization of a eucritic basalt. Proceeding of Lunar Science Conference, 9, 1369-1391.

Walter, J.M., Iezzi, G., Albertini, G., Gunter, M.E., Piochi, M., Ventura, G. Jansen, E., Fiori, F., 1983. Enhanced crystal fabric analysis of a lava flow sample by neutron texture diffraction: A case study from the Castello d'Ischia dome. Geochemistry, Geophysics, Geosystems, 14, 179-196.

Walton E.L., Herd C.D.K., 2007. Dynamic crystallization of shock melts in Allan Hills 77005: Implications for melt pocket formation in Martian meteorites. Geochimica et Cosmochimica Acta, 71, 5267-5285.

Weinberg, M.C., Uhlmann, D.R., Zanotto, E.D., 1989. "Nose method" of calculating critical cooling rates for glass formation. Journal of the American Ceramic Society, 118, 5738-5752.

Weinberg, M.C., 1996. Glass-formation and crystallization kinetics. Thermochimica Acta, 280/281, 63-71.

Whittington, A.G., Hofmeister, A.M., Nabelek, P.I., 2009. Temperature-dependent thermal diffusivity of Earth's crust: Implications for crustal anatexis. Nature, 458, 319-321.

Wohletz, K., Civetta, L., Orsi, G., 1999. Thermal evolution of the Phlegraean magmatic system. Journal of Volcanology and Geothermal Research, 91, 381-414.

Xu, Z., Zhang, Y., 2002. Quench rates in water, air and liquid nitrogen and inference of temperature in volcanic eruption columns. Earth and Planetary Science Letters, 200, 315-330.

Zanotto, E.D., 2010. A bright future for glass-ceramics. American Ceramic Society Bulletin, 89, 19-27.

Zhang, Y., 2008. Geochemical Kinetic. Princeton University Press, Princeton, NY.

Zhou, W., Van der Voo, R., Peacor, D.R., Zhang, Y., 2000. Variable Ti-content and grain size of titanomagnetite as a function of cooling rate in very young MORB. Earth and Planetary Science Letters, 179, 9-20.

TABLES:

Table 1. Chemical compositions and physico-chemical features of the starting materials.

label	SiO_2	TiO_2	Al_2O_3	Fe_2O_3	MnO	MgO	CaO	Na_2O	K_2O	P_2O_5	total Fe_2O_3	H_2O (ppm)	Fe^{2+}/Fe^{total}	density (g/cm³)	Tm (°C)	Tg^* (°C)	Trg	NBO/T	$F^{\#}$
B_{100}	48.02 (0.40)	0.98 (0.08)	15.59 (0.19)	11.37 (0.25)	0.18 (0.04)	9.42 (0.11)	13.20 (0.14)	1.79 (0.05)	0.04 (0.01)	0.06 (0.02)	100.65 (0.67)	53 (13)	0.386 (0.015)	2.757	1233	633	0.51	0.46	0.63
$B_{80}R_{20}$	53.01 (0.30)	0.80 (0.06)	14.99 (0.12)	9.49 (0.17)	0.15 (0.04)	7.58 (0.10)	10.79 (0.16)	2.18 (0.07)	1.02 (0.03)	0.02 (0.02)	100.04 (0.36)	157 (7)	0.449 (0.018)	2.672	1193	639	0.54	0.36	0.59
$B_{60}R_{40}$	57.97 (0.44)	0.65 (0.06)	14.62 (0.27)	7.73 (0.16)	0.13 (0.03)	5.81 (0.08)	8.46 (0.13)	2.59 (0.07)	1.99 (0.05)	0.04 (0.02)	99.99 (0.46)	204 (8)	0.434 (0.021)	2.600	1170	677	0.58	0.26	0.52
$B_{40}R_{60}$	62.73 (0.54)	0.46 (0.05)	14.05 (0.17)	6.02 (0.15)	0.12 (0.04)	4.01 (0.05)	6.07 (0.14)	2.95 (0.07)	3.02 (0.04)	0.02 (0.02)	99.45 (0.73)	238 (4)	0.412 (0.019)	2.525	1144	690	0.60	0.17	0.41
$B_{20}R_{80}$	67.91 (0.38)	0.29 (0.05)	13.59 (0.21)	4.10 (0.20)	0.11 (0.03)	2.18 (0.09)	3.63 (0.13)	3.29 (0.07)	3.99 (0.06)	0.02 (0.02)	99.10 (0.36)	384 (20)	0.424 (0.040)	2.454	1097	709	0.65	0.08	0.24
R_{100}	73.97 (0.67)	0.12 (0.06)	13.48 (0.17)	2.29 (0.16)	0.08 (0.05)	0.44 (0.05)	1.36 (0.08)	3.75 (0.17)	4.89 (0.08)	0.03 (0.02)	100.41 (0.84)	250 (85)	0.342 (0.018)	2.368	1038	760	0.73	0.01	0.03

Footnotes: average and standard deviation values are obtained on at least 15 EPMA point analyses; duplicated Fe^{2+}/Fe_{tot} was determined for each sample using a modified Wilson method as described in Vetere et al., 2013; H_2O content was measured by IR spectroscopy using the peak height of the absorption band at 3550 cm^{-1} (Vetere et al., 2013); density was estimated using the model of Klöß (2000) already reported in Vetere et al., 2013; *Tg (°C at 10^{12} Pas) reported is calculated using the general viscosity model from Huy and Zhang (2006). [#]The kinetic fragility term F for all the selected compositions has been calculated according to F = -0.0044 + 0.6887 (1 - e$^{-5.4767\ NBO/T}$) (Giordano and Dingwell, 2003). The NBO/T values were all calculated by considering total iron as Fe_2O_3.

Table 2. Labels of experiments, thermal paths, numbers of run-products and bulk compositions.

experiment		E-quench	E-9000	E-1800a	E-1800b	E-180a	E-180b	E-60	E-7	E-1a	E-1b
heating rate (°C/h, °C/min)		420, 7									
heat treatment before the onset of cooling		2h at 1300 °C → quenching	→ 2 h at 1300 °C → cooling rate → 800 °C quenching			→ 0.5 h at 1400 °C → 40 h at 1300 °C → cooling rate → 800 °C quenching	→ 2 h at 1300 °C → cooling rate → 800 °C quenching				
cooling rate 1300 - 800 °C	(°C/min) (°C/h)	≥ 15000 $\geq 10^5$	150 9000	30 1800	30 1800	3 180	3 180	1 60	0.117 7	0.00167 1	0.00167 1
experimental time	(min) (h)	190 3.17	305.3 5.08	319 5.32	319 5.32	2867 47.78	26 8.76	802 13.36	4537 75.62	30642 510.70	30642 510.70
number of run-products per experiment		6	3	5	5	6	6	6	6	6	6
bulk compositions investigated		B_{100}, $B_{80}R_{20}$, $B_{60}R_{40}$, $B_{40}R_{60}$, $B_{20}R_{80}$, R_{100}	B_{100}, $B_{80}R_{20}$ $B_{60}R_{40}$	B_{100}, $B_{80}R_{20}$, $B_{60}R_{40}$, $B_{40}R_{60}$ $B_{20}R_{80}$		B_{100}, $B_{80}R_{20}$, $B_{60}R_{40}$, $B_{40}R_{60}$, $B_{20}R_{80}$, R_{100}					

Footnotes: GFA features come from the analysis of 55 run-products (49 + 6). The six run-products of the E-quench experiment were quenched at 1300 °C in order to obtain the physico-chemical characteristics of silicate melts before the onset of cooling.

Table 3. Phase proportions (areas%) determined through image analysis.

bulk composition	experiment	cooling rate °C/h	glass	cpx	sp	plg	crystals	textural features
B$_{100}$ (9 + 1 run-products)	**E-quench**	**≥10^5**	**100**	**0**	**0**	**0**	**0**	**-**
	E-9000	**9000**	**98.0**	**0**	***2.0 (1.2)**	**0**	**2.0 (1.2)**	**H, P**
	E-1800a	1800	34.3	61.0 (2.0)	4.7 (1.2)	0	65.7 (2.1)	H, P
	E-1800b	**1800**	**43.7**	**53.3 (2.2)**	**3.0 (0.7)**	**0**	**56.3 (2.6)**	**H, P**
	E-180a	180	39.6	56.4 (5.0)	4.0 (2.3)	0	60.4 (2.8)	H, P
	E-180b	**180**	**43.3**	**51.2 (1.4)**	**5.4 (1.2)**	**0**	**56.7 (1.6)**	**H, P**
	E-60	**60**	**2.4**	**47.0 (3.2)**	**4.6 (0.6)**	**46.1 (2.4)**	**97.6 (0.8)**	**H, P**
	E-7	**7**	**0.0**	**34.8 (3.6)**	**3.6 (0.9)**	**61.6 (3.1)**	**100.0**	**H, P**
	E-1a	1	0.0	36.2 (10.6)	2.4 (1.4)	61.4 (10.5)	100.0	H, P
	E1-b	**1**	**0.0**	**33.5 (3.9)**	**4.3 (1.8)**	**61.7 (5.0)**	**99.0 (2.2)**	**H, P**
B$_{80}$R$_{20}$ (8 + 1 run-products)	**E-quench**	**≥10^5**	**100**	**0**	**0**	**0**	**0**	**-**
	E-9000	**9000**	**99.4**	**0**	**0.6 (0.2)**	**0**	**0.6 (0.2)**	**H, P**
	E-1800	**1800**	**74.4**	**23.8 (9.5)**	**1.8 (0.6)**	**0**	**25.6 (9.9)**	**IN, P**
	E-180a	180	51.6	47.3 (3.4)	1.2 (0.8)	0	48.4 (2.6)	H, P
	E-180b	**180**	**51.6**	**45.9 (1.9)**	**2.6 (1.4)**	**0**	**48.4 (2.1)**	**H, P**
	E-60	**60**	**59.0**	**39.2 (2.8)**	**1.7 (0.9)**	**0**	**41.0 (1.9)**	**H, P**
	E-7	**7**	**65.3**	**31.1 (4.1)**	**2.9 (1.0)**	**0.8 (0.8)**	**34.7 (4.2)**	**IN, P**
	E-1a	**1**	**22.3**	**24.3 (1.9)**	**3.3 (1.0)**	**50.2 (4.6)**	**77.7 (2.5)**	**H, P**
	E1-b	1	24.0	26.2 (0.2)	1.0 (0.6)	48.8 (3.9)	76.0 (3.8)	**H, P**
B$_{60}$R$_{40}$ (8 + 1 run-products)	**E-quench**	**≥10^5**	**100**	**0**	**0**	**0**	**0**	**-**
	E-9000	**9000**	**100**	**0**	**0.5 (0.3)**	**0**	**0.5 (0.3)**	**H, P**
	E-1800	**1800**	**97.3**	**2.1 (1.6)**	**0.5 (0.4)**	**0**	**2.7 (2.0)**	**H, P**
	E-180a	180	66.7	30.3 (3.9)	3.0 (1.0)	0	33.3 (3.9)	H, P
	E-180b	**180**	**70.1**	**28.5 (2.7)**	**1.4 (1.2)**	**0**	**29.9 (3.8)**	**H, P**
	E-60	**60**	**67.1**	**30.3 (2.9)**	**2.6 (1.6)**	**0**	**32.9 (2.1)**	**H, P**
	E-7	**7**	**41.6**	**21.5 (1.8)**	**2.8 (1.0)**	**34.1 (6.8)**	**58.4 (7.0)**	**IN, P**
	E-1a	**1**	**42.4**	**17.3 (5.2)**	**2.1 (0.7)**	**38.2 (6.7)**	**57.6 (3.9)**	**H, P**
	E1-b	1	36.3	21.5 (12.0)	1.8 (1.0)	40.4 (9.2)	63.7 (6.7)	IN, P
B$_{40}$R$_{60}$ (7 + 1 run-products)	**E-quench**	**≥10^5**	**100**	**0**	**0**	**0**	**0**	**-**
	E-1800	**1800**	**99.5**	**0**	**0.5 (0.1)**	**0**	**0.5 (0.1)**	**IN, A**
	E-180a	180	96.3	3.3 (2.9)	0.3 (0.3)	0	3.7 (3.3)	H, A
	E-180b	**180**	**96.2**	**3.4 (1.9)**	**0.5 (0.3)**	**0**	**3.8 (2.2)**	**H, A**
	E-60	**60**	**79.7**	**19.5 (3.2)**	**0.7 (0.4)**	**0**	**20.3 (3.4)**	**H, A**
	E-7	**7**	**82.1**	**16.6 (4.4)**	**2.0 (0.4)**	**0**	**17.9 (4.1)**	**IN, A**
	E-1a	**1**	**80.7**	**15.7 (3.7)**	**1.3 (0.4)**	**2.2 (1.2)**	**19.3 (3.3)**	**H, A**
	E-1b	1	67.1	11.4 (4.3)	1.5 (0.9)	20 (12.6)	32.9 (10.9)	IN, A

	E-quench	$\geq 10^5$	100	**0**	**0**	**0**	**0**	-
	E-1800	1800	**99.5**	**0**	**0.5 (0.2)**	**0**	**0.5 (0.2)**	**H, A**
	E-180a	180	99.4	0	0.4 (0.2)	0	0.6 (0.2)	H, A
$B_{20}R_{80}$	**E-180b**	**180**	**99.8**	**0**	**0.2 (0.1)**	**0**	**0.2 (0.1)**	**H, A**
(7 + 1 run-products)	**E-60**	**60**	**98.8**	**0**	***1.2 (0.2)**	**0**	**1.2 (0.2)**	**H, A**
	E-7	**7**	**98.0**	**1.7 (0.8)**	**0.3 (0.3)**	**0**	**2.0 (1.1)**	**H, A**
	E-1a	1	87.7	10.3 (2.0)	1.7 (1.5)	0	12.3 (2.7)	H, A
	E1-b	**1**	**91.3**	**8.5 (1.4)**	**0.3 (0.1)**	**0**	**8.7 (1.4)**	**H, A**
	E-quench	$\geq 10^5$	**100**	**0**	**0**	**0**	**0**	-
	E-180a	**180**	**100**	**0**	**0**	**0**	**0**	-
R_{100}	**E-180b**	**180**	**100**	**0**	**0**	**0**	**0**	-
(6 + 1	**E-60**	**60**	**100**	**0**	**0**	**0**	**0**	-
run-products)	**E-7**	**7**	**100**	**0**	**0**	**0**	**0**	-
	E-1a	**1**	**99.0**	**0**	**1.0 (0.1)**	**0**	**1.0 (0.1)**	H, A
	E1-b	1	98.5	0	1.5 (0.1)	0	1.5 (0.1)	**H, A**

Footnotes. Phase contents were measured as the average of 3 to 36 BS-SEM images per run-product; we analysed about 500 BS-SEM images. Following Vetere et al. (2013), H and IN indicate the homogeneous and inhomogeneous distributions of crystals inside a run-product, i.e. samples with standard deviations of crystalline contents ≤ and > 4 area%, respectively; P and A indicate the preferential nucleation (mainly for sp) and the absence of preferential nucleation on Pt-capsules, respectively; between two run-products cooled at the same rate, we considered more reliable that with the lowest crystal content and standard deviation (homogeneous); the run-products considered more reliable are in bold and plotted in Fig. 4 and 5. The run-products E-1800 for $B_{80}R_{20}$ and E-7 for $B_{60}R_{40}$ with high standard deviations are plotted in Fig. 4 and 5. *In these run-products cpx and sp are measured together due to the fact that are not clearly distinguishable.

Table 4. Average chemical compositions (wt. %) of matrix (> 50 μm from crystals) and intracrystalline (< 50 μm from crystals) glasses determined by SEM-EDS and EPMA-WDS.

bulk composition	experiment	analytical method of matrix and intracrystalline glasses	Crystals (area %)	SiO$_2$	TiO$_2$	Al$_2$O$_3$	Fe$_2$O$_3$	MnO	MgO	CaO	Na$_2$O	K$_2$O	Total Fe$_2$O$_3$
B$_{100}$	E-9000	EPMA - matrix	2.0 (1.2)	48.90 (0.50)	0.99 (0.08)	15.47 (0.22)	10.84 (0.14)	0.16 (0.04)	9.74 (0.13)	12.96 (0.07)	1.99 (0.07)	0.04 (0.01)	101.09 (0.55)
	E-9000	SEM -matrix	2.0 (1.2)	47.00 (0.42)	0.98 0.25)	15.99 (0.26)	10.97 (1.38)	0.24 (0.19)	9.87 (0.22)	12.39 (0.28)	1.94 (0.18)	0.08 (0.07)	99.47 (1.37)
	E-1800b	SEM - intracrystalline	56.3 (2.6)	58.05 (1.19)	0.82 (0.22)	20.07 (0.71)	6.74 (1.52)	0.17 (0.26)	2.75 (0.40)	6.86 (0.59)	3.28 (0.21)	0.22(0.13)	99.03 (1.41)
	E-180b	EPMA - intracrystalline	56.7 (1.6)	59.02 (0.68)	0.84 (0.12)	19.92 (0.95)	4.10 (0.79)	0.17 (0.04)	3.59 (0.59)	7.93 (0.40)	3.96 (0.68)	0.21 (0.03)	99.74 (0.29)
	E-60	-	97.6 (0.8)	-	-	-	-	-	-	-	-	-	-
	E-7	-	100.0	-	-	-	-	-	-	-	-	-	-
	E1-b	-	99.0 (2.2)	-	-	-	-	-	-	-	-	-	-
B$_{80}$R$_{20}$	E-9000	EPMA - matrix	0.6 (0.2)	53.59 (0.33)	0.78 (0.08)	14.88 (0.15)	9.28 (0.19)	0.16 (0.06)	7.88 (0.13)	10.69 (0.21)	2.43 (0.10)	0.90 (0.02)	100.58 (0.44)
	E-1800	EPMA - matrix	25.6 (9.9)	53.92 (0.66)	0.76 (0.07)	15.20 (0.25)	9.13 (0.24)	0.15 (0.04)	7.84 (0.16)	10.83 (0.18)	2.28 (0.10)	0.88 (0.04)	100.99 (0.76)
	E-1800	SEM - matrix	25.6 (9.9)	51.87 (0.54)	0.95 (0.45)	15.42 (0.40)	8.26 (0.92)	0.46 (0.32)	7.96 (0.36)	10.22 (0.68)	2.29 (0.17)	1.07 (0.30)	98.50 (1.37)
	E-180b	EPMA - matrix	48.4 (2.1)	53.33 (0.27)	0.82 (0.04)	15.03 (0.27)	9.56 (0.17)	0.18 (0.03)	7.79 (0.14)	10.87 (0.37)	1.96 (0.10)	0.65 (0.18)	100.19 (0.20)
	E-180b	EPMA - intracrystalline	48.4 (2.1)	61.18 (0.25)	0.73 (0.14)	19.88 (0.25)	3.75 (0.12)	0.09 (0.01)	2.42 (0.06)	5.67 (0.23)	4.62 (0.15)	1.76 (0.02)	100.09 (0.10)
	E-60	SEM - intracrystalline	41.0 (1.9)	61.05 (1.22)	0.88 (0.40)	20.78 (0.44)	4.00 (0.97)	0.29 (0.21)	2.42 (0.19)	6.61 (0.62)	3.44 (0.30)	1.77 (0.28)	101.24 (1.81)
	E-7	EPMA -intracrystalline	34.7 (4.2)	63.91 (0.73)	0.76 (0.14)	19.43 (0.38)	2.69 (0.42)	0.07 (0.03)	1.91 (0.24)	5.34 (0.36)	4.69 (0.14)	1.91 (0.08)	100.72 (0.38)
	E-1a	EPMA -intracrystalline	77.7 (2.5)	73.05 (0.71)	1.60 (0.14)	11.79 (0.33)	1.77 (0.22)	0.03 (0.02)	0.43 (0.10)	1.20 (0.15)	2.37 (0.41)	4.45 (0.11)	98.20 (0.95)
B$_{60}$R$_{40}$	E-9000	EPMA - matrix	0.5 (0.3)	57.69 (0.56)	0.66 (0.09)	15.03 (0.27)	7.05 (0.29)	0.16 (0.06)	5.78 (0.13)	8.51 (0.22)	3.37 (0.13)	2.14 (0.06)	100.40 (0.36)
	E-1800a	EPMA - matrix	2.7 (2.0)	58.07 (0.29)	0.63 (0.07)	14.78 (0.30)	7.38 (0.24)	0.13 (0.04)	5.73 (0.07)	8.40 (0.09)	3.23 (0.14)	1.86 (0.12)	100.21 (0.62)
	E-1800a	SEM - matrix	2.7 (2.0)	58.80 (0.57)	1.06 (0.50)	14.95 (0.48)	7.31 (0.76)	0.49 (0.32)	6.18 (0.21)	8.08 (0.29)	2.51 (0.26)	2.22 (0.39)	101.59 (1.53)
	E-180b	EPMA -intracrystalline	29.9 (3.8)	61.46 (2.14)	0.72 (0.12)	15.95 (1.02)	6.94 (1.40)	0.16 (0.04)	4.18 (1.49)	7.31 (1.61)	2.89 (0.62)	1.92 (0.62)	101.53 (0.32)
	E-60	SEM -intracrystalline	32.9 (2.1)	63.26 (1.22)	0.65 (0.32)	19.67 (0.46)	4.18 (1.09)	0.19 (0.15)	1.96 (0.25)	5.68 (0.43)	3.28 (0.25)	2.70 (0.22)	101.56 (1.26)
	E-7	EPMA -intracrystalline	58.4 (7.0)	65.27 (0.82)	0.63 (0.11)	18.56 (0.45)	2.69 (0.19)	0.08 (0.05)	1.35 (0.07)	4.49 (0.21)	3.69 (0.18)	3.25 (0.09)	100.01 (0.50)
	E-1a	EPMA -intracrystalline	57.6 (6.3)	73.48 (1.18)	1.15 (0.19)	11.52 (0.30)	2.49 (0.45)	0.08 (0.03)	0.42 (0.05)	1.13 (0.14)	2.89 (0.23)	4.90 (0.11)	98.07 (1.38)
B$_{40}$R$_{60}$	E-1800a	EPMA - matrix	0.5 (0.1)	63.48 (0.80)	0.47 (0.05)	14.44 (0.20)	5.35 (0.35)	0.10 (0.04)	3.91 (0.17)	6.13 (0.17)	3.88 (0.19)	3.06 (0.10)	100.82 (0.79)
	E-180b	EPMA - matrix	3.8 (2.2)	63.86 (0.39)	0.50 (0.11)	14.33 (0.20)	5.68 (0.15)	0.10 (0.05)	3.98 (0.08)	6.03 (0.17)	3.15 (0.08)	2.96 (0.06)	100.58 (0.48)
	E-60	SEM -intracrystalline	20.3 (3.4)	66.71 (1.24)	0.60 (0.36)	16.57 (0.44)	5.11 (1.78)	0.21 (0.15)	1.29 (0.22)	3.56 (0.48)	2.84 (0.17)	3.50 (0.37)	100.38 (1.52)

	E-7	EPMA -intracrystalline	17.9 (4.1)	66.95 (0.72)	0.51 (0.06)	16.11 (0.37)	4.12 (0.89)	0.08 (0.05)	1.52 (0.35)	4.45 (0.40)	3.35 (0.12)	3.26 (0.19)	100.35 (0.85)
	E-1a	EPMA -intracrystalline	19.3 (3.3)	67.45 (1.19)	0.43 (0.08)	16.81 (0.28)	2.77 (0.39)	0.09 (0.04)	1.10 (0.14)	3.86 (0.24)	3.92 (0.17)	3.48 (0.13)	99.90 (1.08)
$B_{20}R_{80}$	E-1800a	EPMA - matrix	0.5 (0.2)	68.25 (0.78)	0.27 (0.04)	12.77 (0.19)	3.81 (0.18)	0.09 (0.04)	2.12 (0.08)	3.51 (0.18)	4.41 (0.12)	3.60 (0.07)	98.83 (0.92)
	E-180b	EPMA - matrix	0.2 (0.1)	68.47 (0.80)	0.31 (0.06)	13.96 (0.44)	3.85 (0.16)	0.09 (0.04)	2.17 (0.05)	3.69 (0.16)	3.52 (0.11)	3.92 (0.07)	99.96 (0.45)
	E-60	EPMA - matrix	1.2 (0.2)	69.81 (1.49)	0.27 (0.10)	14.54 (0.44)	3.39 (0.80)	0.13 (0.10)	1.75 (0.72)	3.16 (0.77)	3.15 (0.42)	4.42 (0.53)	100.62 (0.91)
	E-7	EPMA - matrix	2.0 (1.1)	68.50 (0.47)	0.28 (0.02)	13.89 (0.18)	3.90 (0.23)	0.08 (0.04)	2.20 (0.07)	3.38 (0.09)	3.38 (0.09)	3.74 (0.08)	99.86 (0.84)
	E1-b	SEM - intracrystalline	8.7 (1.4)	72.85 (1.81)	0.27 (0.20)	15.63 (0.55)	2.28 (0.95)	0.012 (0.15)	0.67 (0.18)	1.96 (0.36)	3.33 (0.38)	4.26 (0.44)	101.76 (1.68)
R_{100}	E-180a	EPMA - matrix	0	72.92 (0.36)	0.13 (0.03)	13.04 (0.17)	2.15 (0.11)	0.08 (0.05)	0.45 (0.02)	1.38 (0.04)	3.82 (0.08)	4.90 (0.02)	98.86 (0.39)
	E-180b	EPMA - matrix	0	73.53 (0.78)	0.14 (0.04)	13.20 (0.15)	2.28 (0.11)	0.06 (0.04)	0.44 (0.04)	1.31 (0.08)	3.80 (0.10)	4.98 (0.07)	99.73 (0.71)
	E-60	SEM - matrix	0	75.37 (0.95)	0.16 (0.12)	13.68 (0.34)	1.97 (0.32)	0.34 (0.22)	0.60 (0.15)	1.14 (0.26)	3.21 (0.15)	4.65 (0.39)	101.17 (1.22)
	E-7	EPMA - matrix	0	73.94 (0.48)	0.12 (0.07)	13.38 (0.19)	2.12 (0.07)	0.07 (0.03)	0.43 (0.04)	1.35 (0.06)	3.81 (0.06)	4.85 (0.06)	100.09 (0.60)
	E-1a	SEM - matrix	1.0 (0.1)	74.58 (0.84)	0.22 (0.16)	13.82 (0.51)	1.63 (0.40)	0.21 (0.14)	0.47 (0.24)	1.20 (0.28)	3.42 (0.24)	5.47 (0.36)	101.04 (0.66)

Footnotes. Each chemical analysis is the average of at least 5 SEM-EDS and/or EPMA-WDS point analyses, with a total of oxide content comprised between 98 and 102 wt.%.

Table 5. Average chemical compositions (wt. %) of cpx determined by SEM-EDS and EPMA-WDS.

bulk composition	experiment	analytical method	crystals (area %)	cpx (area %)	SiO_2	TiO_2	Al_2O_3	Fe_2O_3	MnO	MgO	CaO	Na_2O	K_2O	Total Fe_2O_3
B_{100}	E-1800b	SEM	56.3 (2.6)	53.3 (2.2)	47.70 (0.92)	0.98 (0.35)	10.39 (1.35)	9.76 (1.06)	0.44 (0.23)	16.75 (2.87)	13.25 (1.03)	0.42 (0.24)	0.28 (0.19)	99.97 (1.84)
	E-180b	EPMA	56.7 (1.6)	51.2 (1.4)	44.37 (0.77)	0.93 (0.09)	10.50 (0.51)	12.64 (1.17)	0.21 (0.05)	14.59 (1.03)	15.96 (1.55)	0.33 (0.10)	0.03 (0.02)	99.52 (0.48)
	E-60	SEM	97.6 (0.8)	47.0 (3.2)	45.95 (1.03)	1.08 (0.41)	11.08 (0.80)	9.04 (1.06)	0.21 (0.18)	15.43 (1.24)	18.83 (0.80)	0.42 (0.13)	0.09 (0.06)	101.85 (1.29)
	E-7	EPMA	100.0	34.8 (3.6)	46.35 (1.43)	1.13 (0.23)	7.07 (1.03)	10.27 (1.00)	0.20 (0.05)	15.11 (1.14)	19.69 (0.77)	0.53 (0.10)	0.02 (0.01)	100.36 (0.34)
	E1-b	EPMA	99.0 (2.2)	33.5 (3.9)	47.12 (1.91)	0.96 (0.28)	5.59 (1.34)	9.07 (1.36)	0.20 (0.07)	14.99 (2.06)	19.95 (1.37)	0.50 (0.11)	0.01 (0.01)	98.37 (0.56)
$B_{80}R_{20}$	E-1800	SEM	25.6 (9.9)	23.8 (9.5)	-	-	-	-	-	-	-	-	-	-
	E-180b	SEM	48.4 (2.1)	45.9 (1.9)	45.25 (1.64)	1.17 (0.34)	11.21 (1.64)	12.77 (1.20)	0.24 (0.15)	11.91 (2.84)	15.33 (1.71)	0.97 (0.43)	0.12 (0.10)	98.97 (0.92)
	E-60	SEM	41.0 (1.9)	39.2 (2.8)	45.90 (1.24)	0.91 (0.36)	9.95 (0.63)	11.57 (1.63)	0.16 (0.14)	15.69 (1.27)	16.57 (1.20)	0.43 (0.19)	0.12 (0.10)	101.29 (1.09)
	E-7	EPMA	34.7 (4.2)	31.1 (4.1)	45.48 (0.82)	0.84 (0.07)	8.56 (0.48)	11.40 (1.27)	0.20 (0.03)	14.71 (0.66)	19.69 (0.61)	0.39 (0.04)	0.03 (0.02)	101.30 (0.57)
	E-1a	EPMA	77.7 (2.5)	24.3 (1.9)	46.15 (0.86)	0.76 (0.08)	8.59 (0.34)	9.46 (0.87)	0.16 (0.06)	14.67 (0.48)	19.67 (0.37)	0.30 (0.03)	0.01 (0.01)	99.78 (0.57)
$B_{60}R_{40}$	E-1800a	-	2.7 (2.0)	2.1 (1.6)	-	-	-	-	-	-	-	-	-	-
	E-180b	-	29.9 (3.8)	28.5 (2.7)	-	-	-	-	-	-	-	-	-	-
	E-60	SEM	32.9 (2.1)	30.3 (2.9)	47.88 (1.04)	0.79 (0.35)	9.71 (0.51)	9.63 (1.00)	0.18 (0.15)	16.13 (1.47)	16.47 (1.43)	0.56 (0.16)	0.24 (0.18)	101.58 (0.76)
	E-7	SEM	58.4 (7.0)	21.5 (1.8)	46.09 (1.79)	0.72 (0.27)	8.38 (1.12)	12.12 (2.20)	0.24 (0.16)	14.56 (1.85)	16.99 (1.43)	0.57 (0.18)	0.12 (0.11)	99.79 (1.89)
	E-1a	EPMA	57.6 (6.3)	17.3 (5.2)	46.27 (1.19)	0.58 (0.13)	7.70 (0.49)	10.68 (1.26)	0.21 (0.04)	14.67 (1.07)	19.30 (0.74)	0.34 (0.04)	0.02 (0.01)	99.77 (0.69)
$B_{40}R_{60}$	E-180b	-	3.8 (2.2)	3.4 (1.9)	-	-	-	-	-	-	-	-	-	-
	E-60	SEM	20.3 (3.4)	19.5 (3.2)	55.17 (1.20)	0.50 (0.31)	10.32 (0.95)	8.81 (0.59)	0.17 (0.12)	13.10 (2.64)	11.93 (1.45)	1.14 (0.38)	0.68 (0.25)	101.81 (1.86)
	E-7	SEM	17.9 (4.1)	16.6 (4.4)	49.05 (1.06)	0.45 (0.27)	7.53 (0.71)	10.64 (0.98)	0.41 (0.32)	14.93 (1.76)	16.47 (1.22)	0.61 (0.20)	0.26 (0.14)	100.35 (1.20)
	E-1a	EPMA	19.3 (3.3)	15.7 (3.7)	45.20 (1.24)	0.58 (0.07)	7.01 (0.43)	11.58 (1.18)	0.26 (0.09)	13.73 (1.38)	19.69 (0.97)	0.38 (0.01)	0.06 (0.01)	98.49 (0.50)
$B_{20}R_{80}$	E-7	-	2.0 (1.1)	1.7 (0.8)	-	-	-	-	-	-	-	-	-	-
	E1-b	SEM	8.7 (1.4)	8.5 (1.4)	47.49 (1.30)	0.70 (0.64)	6.74 (0.60)	8.98 (2.33)	0.26 (0.21)	14.52 (0.98)	19.12 (1.78)	0.74 (0.259)	0.30 (0.16)	98.86 (2.23)

Footnotes. Each chemical analysis reported is the average of at least 5 SEM-EDS and/or EPMA-WDS point analyses, with a total of oxide content comprised between 98 and 102 wt.%.

Table 6. Parameters used for the conductive cooling simulations of B_{100} and R_{100} silicate liquid compositions as a function of lava thickness; simulations were performed with the Heat 3D algorithm (Wholetz, 1999).

melt	thickness of molten silicate (m)	thermal range of simulation (°C)	thermal conductivity K (W/mK)	thermal diffusivity k (mm²/s)	heat capacity C_p (J/kgK)	density ρ (Kg/m³)	grid size (m)	soil thickness (m)
R_{100}	0.5	1300-800	1.5	0.5	1270	2350	0.1	15
	1							
	2							
	3							
	5							
	10							
B_{100}	0.5	1300-800	0.9	0.25	1300	2750	0.1	15
	1							
	2							
	3							
	5							
	10							

Footnotes: thermal conductivity is calculated as $K = k * C_p * \rho$; the physico-chemical parameters are taken from Romine et al. (2012) and Nabelek et al. (2012).

FIGURES
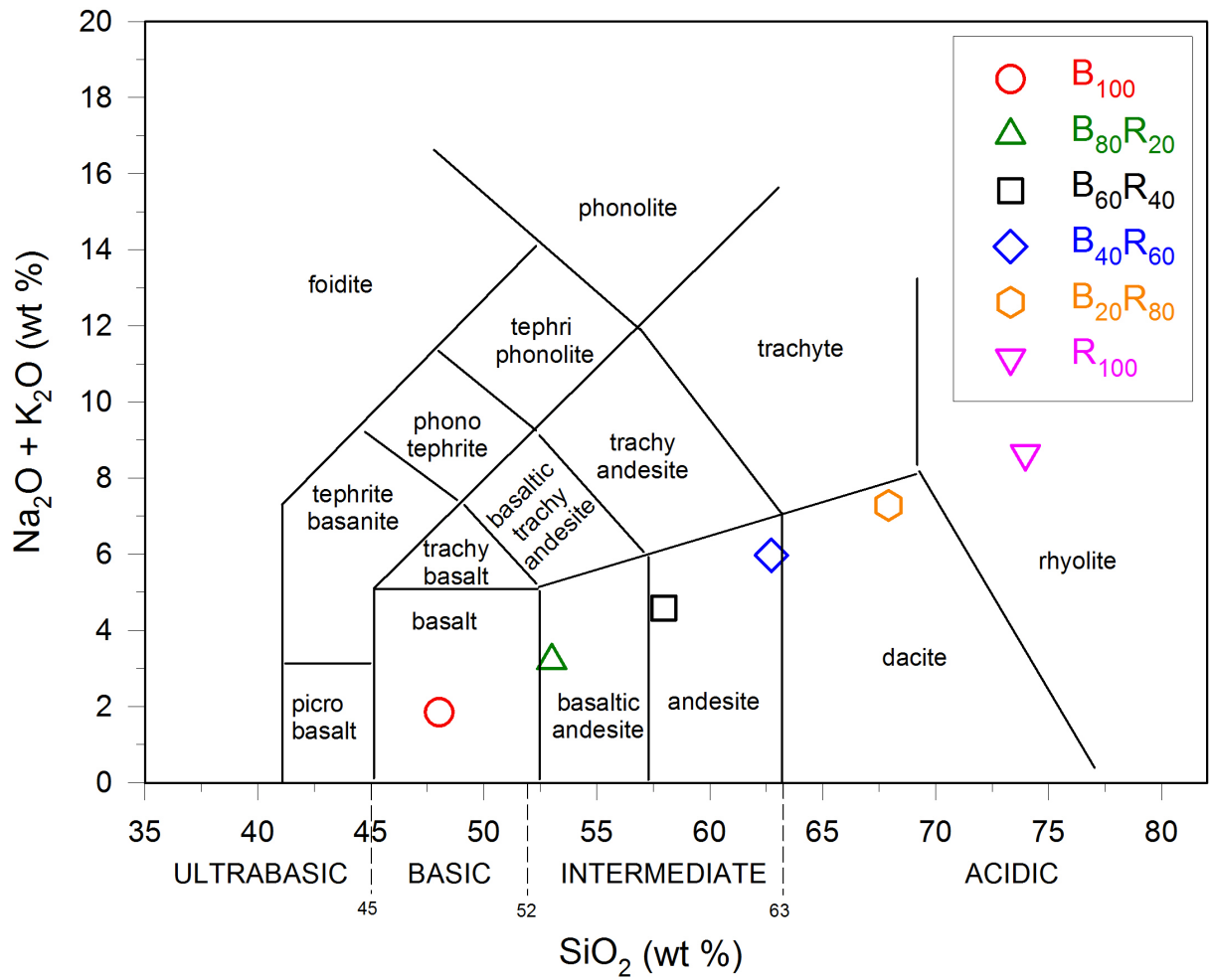
Figure 1. Starting compositions from this study are plotted in the TAS diagram.
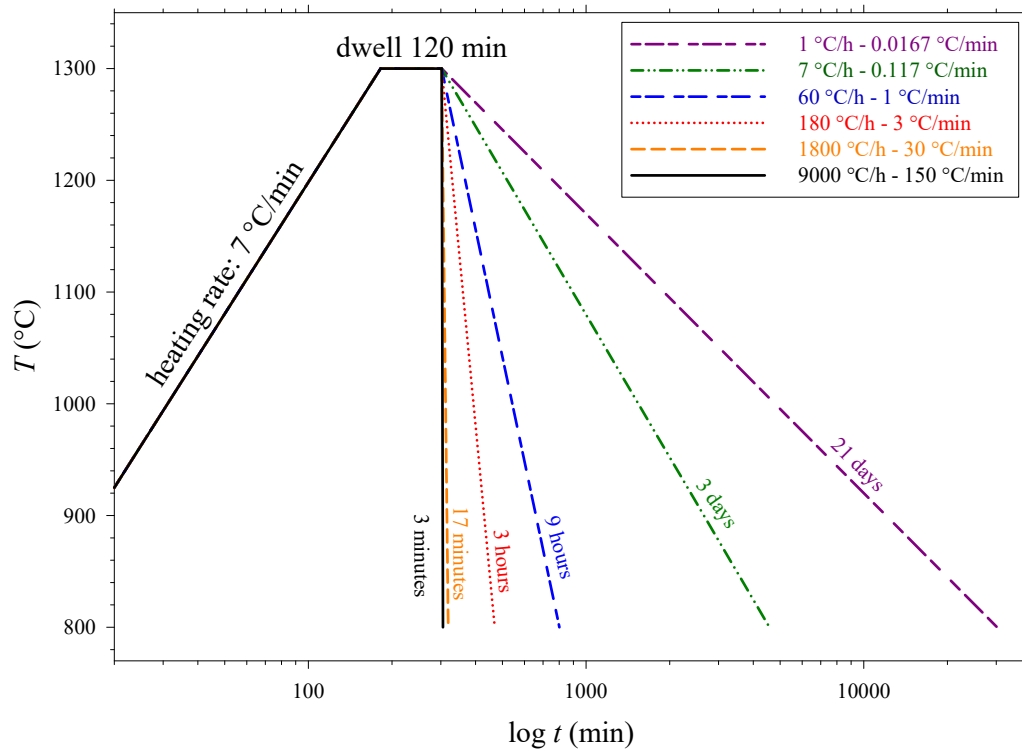
Figure 2. Thermal paths used in this study; the experiment with a heat treatment of 1400 °C and 40 hours at 1300 °C is not reported.
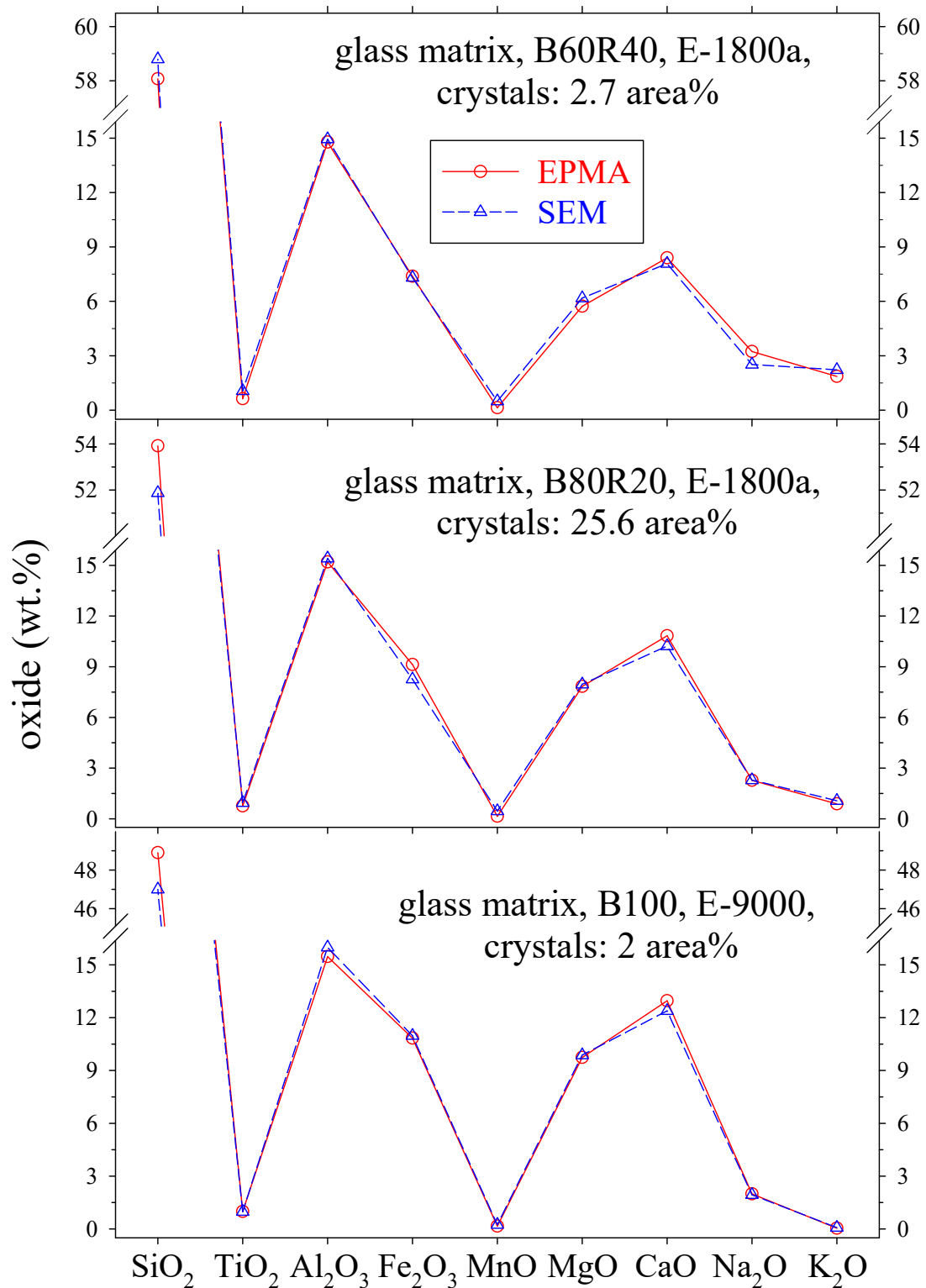
Figure 3. Comparison between average chemical analyses of glasses obtained with SEM and EPMA (see Table 4).
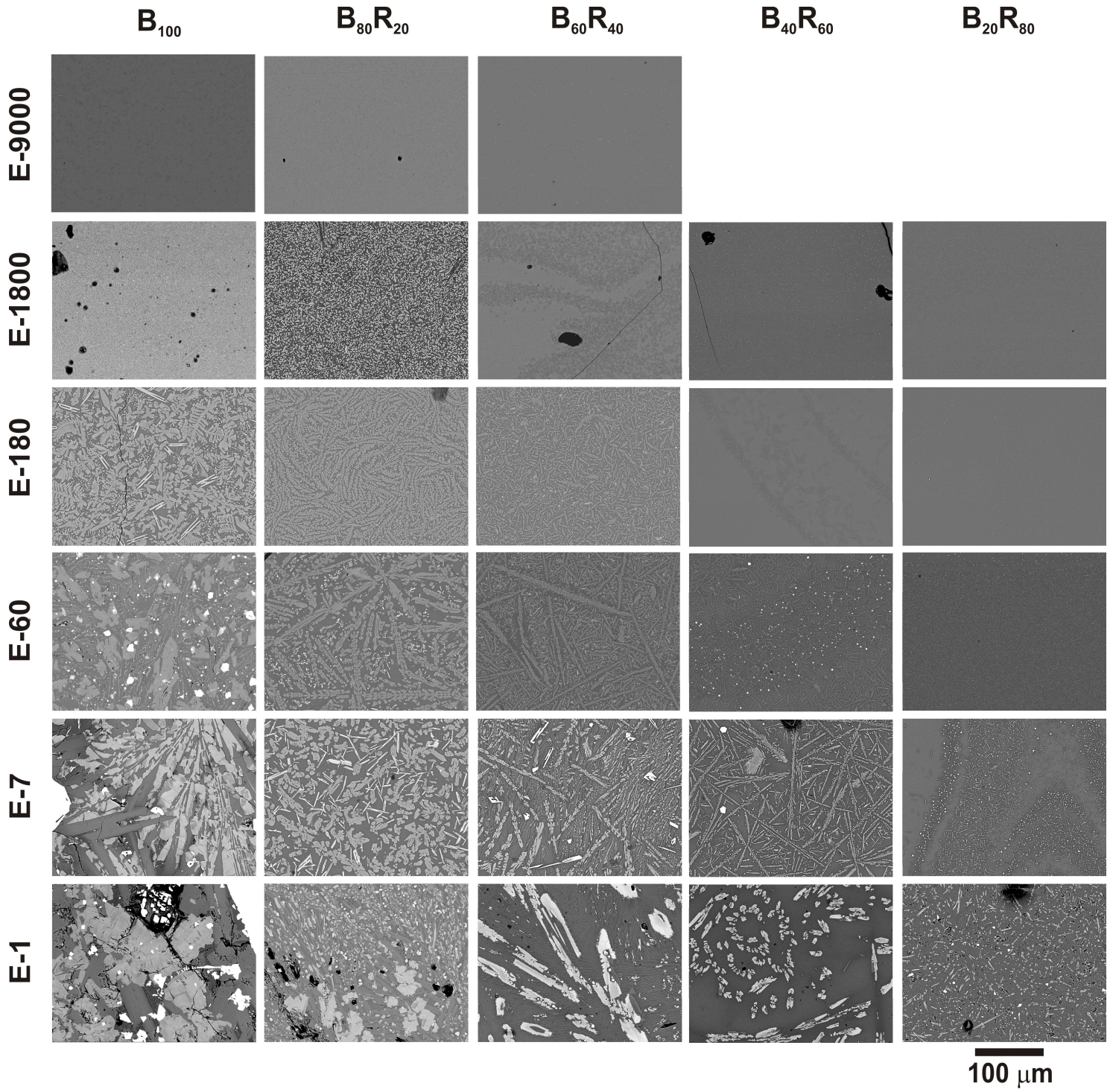
Figure 4a.
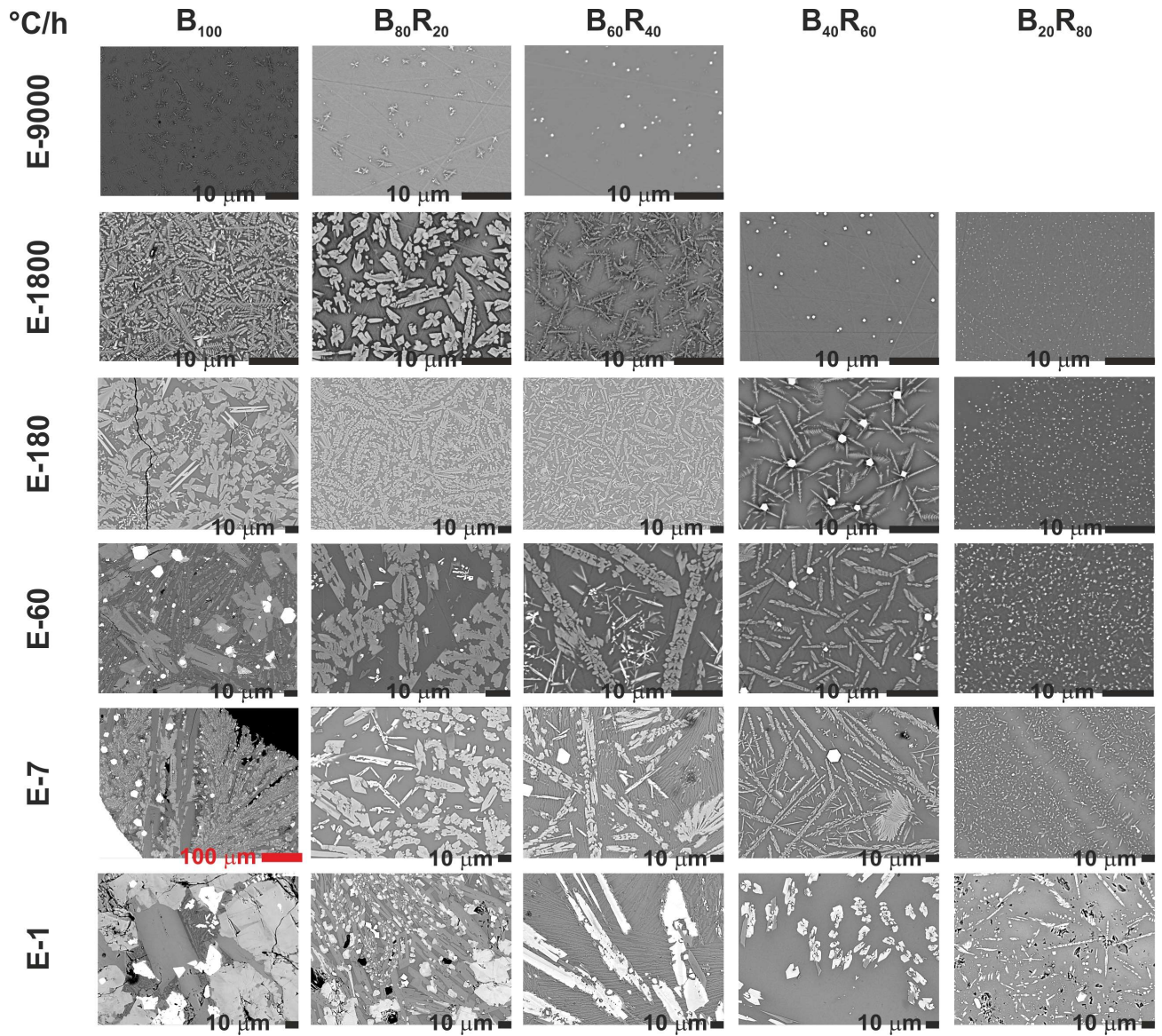
Figure 4b.
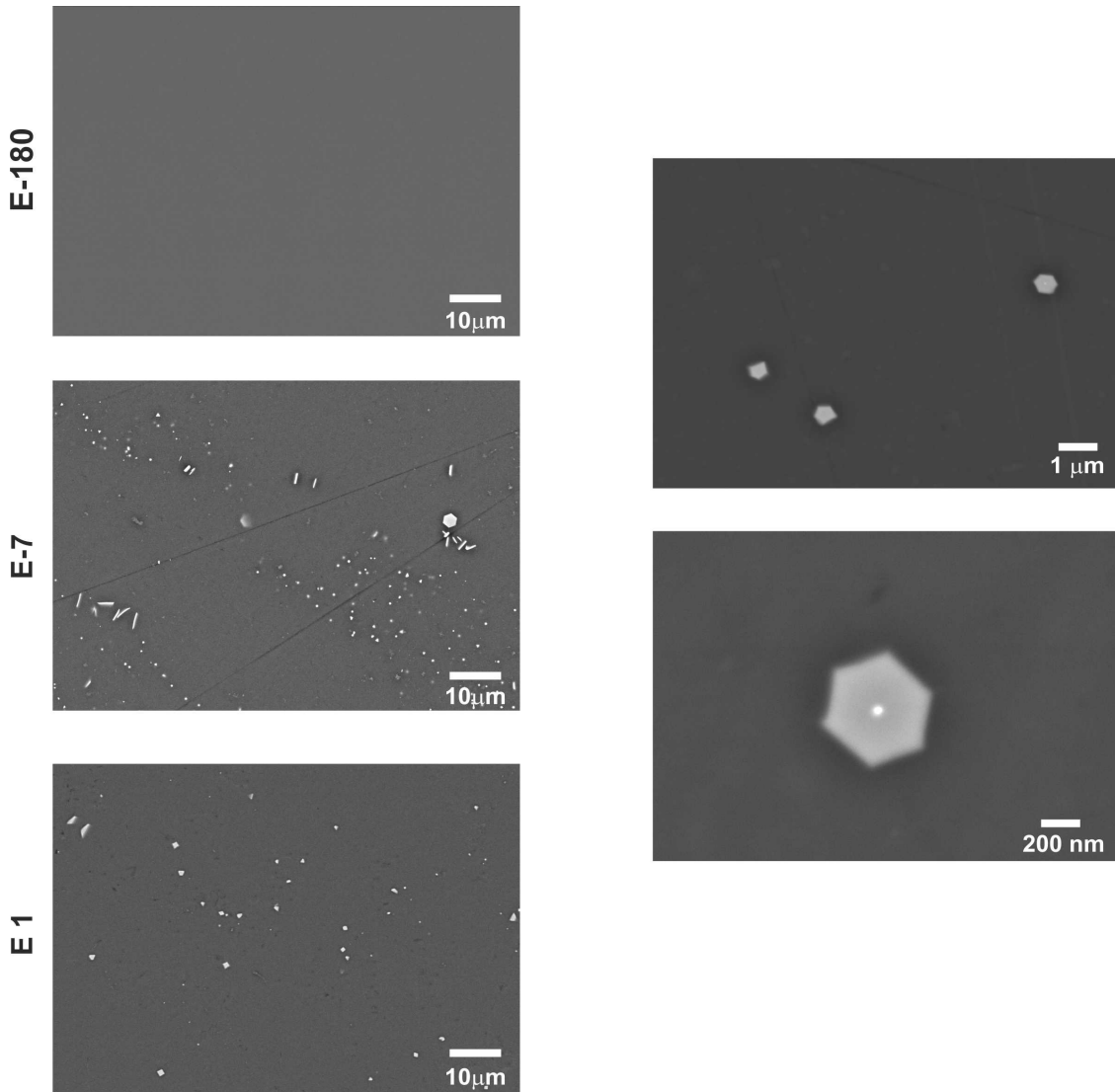
Figure 4c.

Figures 4. a) Overview and comparison of textural features observed with BS-SEM images at the same magnification as a function of bulk composition and cooling rate. b) The most important textural features are evidenced using different magnifications (blue and red bars correspond to 10 and 100 µm, respectively). c) Rhyolite samples from experiments E-180, E-7 and E-1 cooled at 180, 7 and 1 °C/h, respectively; the two microphotographs on the right column are referred to E-1 experiment obtained at 10000 (up) and 50000 x (down).
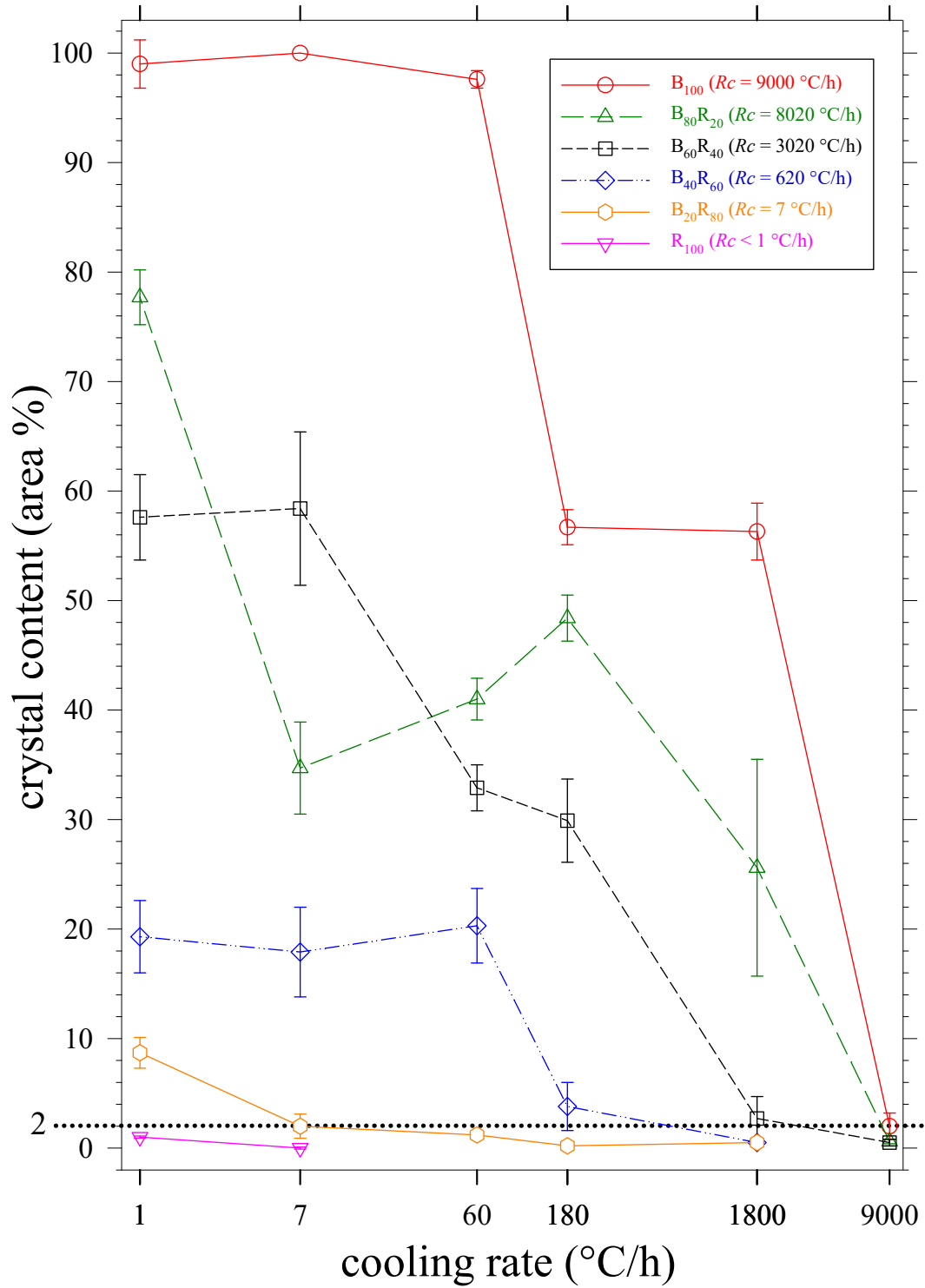
Figure 5. Crystal content of run-products (area %) *vs* cooling rate (°C/h). The horizontal dotted line at 2 area% of crystals correspond to the critical cooling rate *Rc*.
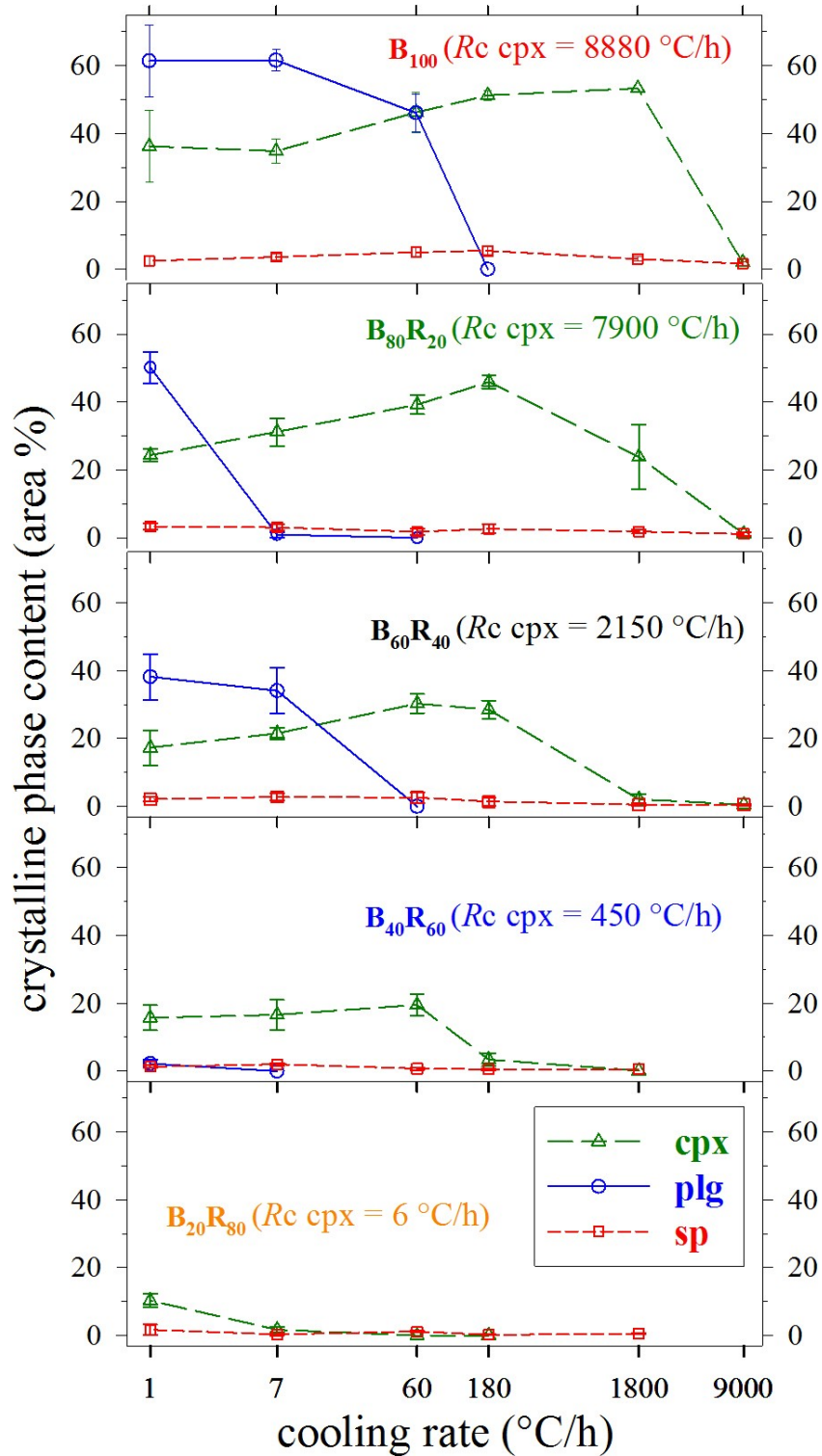
Figure 6. Evolution of plg, cpx and sp contents (area%) for each starting composition; the rate of cooling that solidifies 2 area % of cpx is also showed.
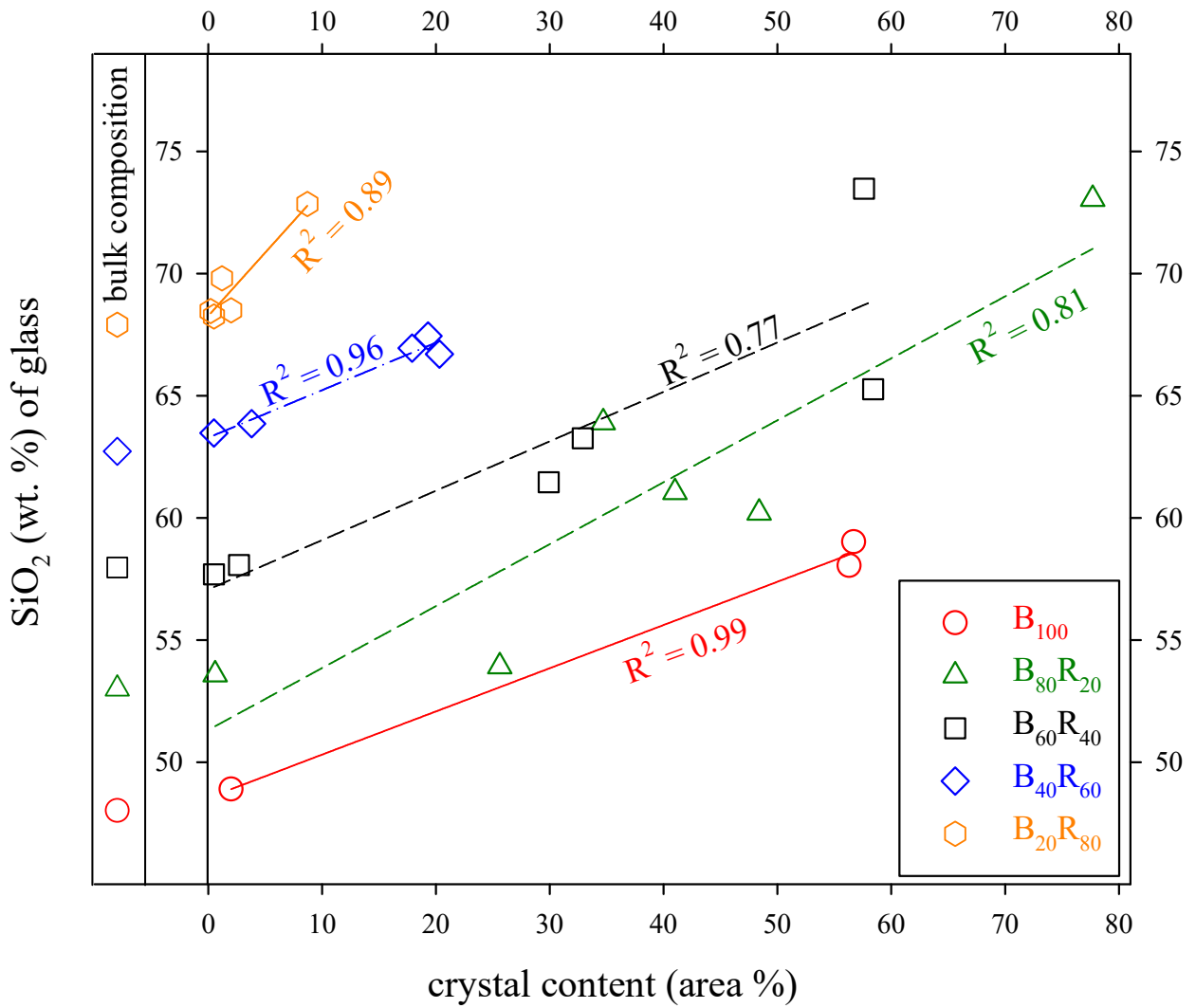
Figure 7. Evolution of SiO_2 in glass matrix (measured at distance > 50 μm from crystals) as a function of crystal content; R_{100} is not showed.
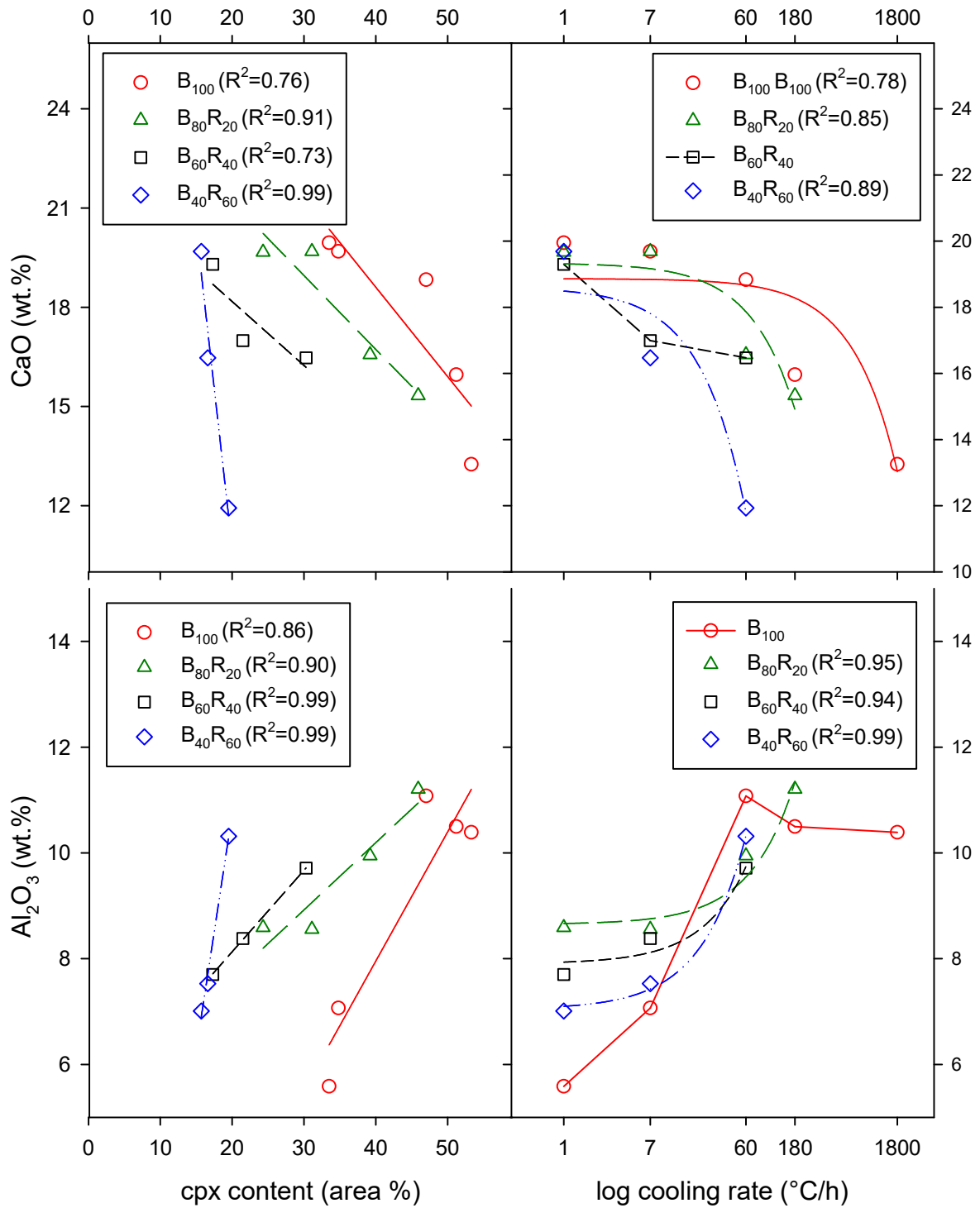
Figure 8. Variation of Al_2O_3 and CaO of the melt as a function of cpx content (left diagrams) and cooling rate (right diagrams). The lines trough Al_2O_3 content for B_{100} and CaO content for $B_{40}R_{60}$ are plotted as guide for eye; the other lines are linear regressions.
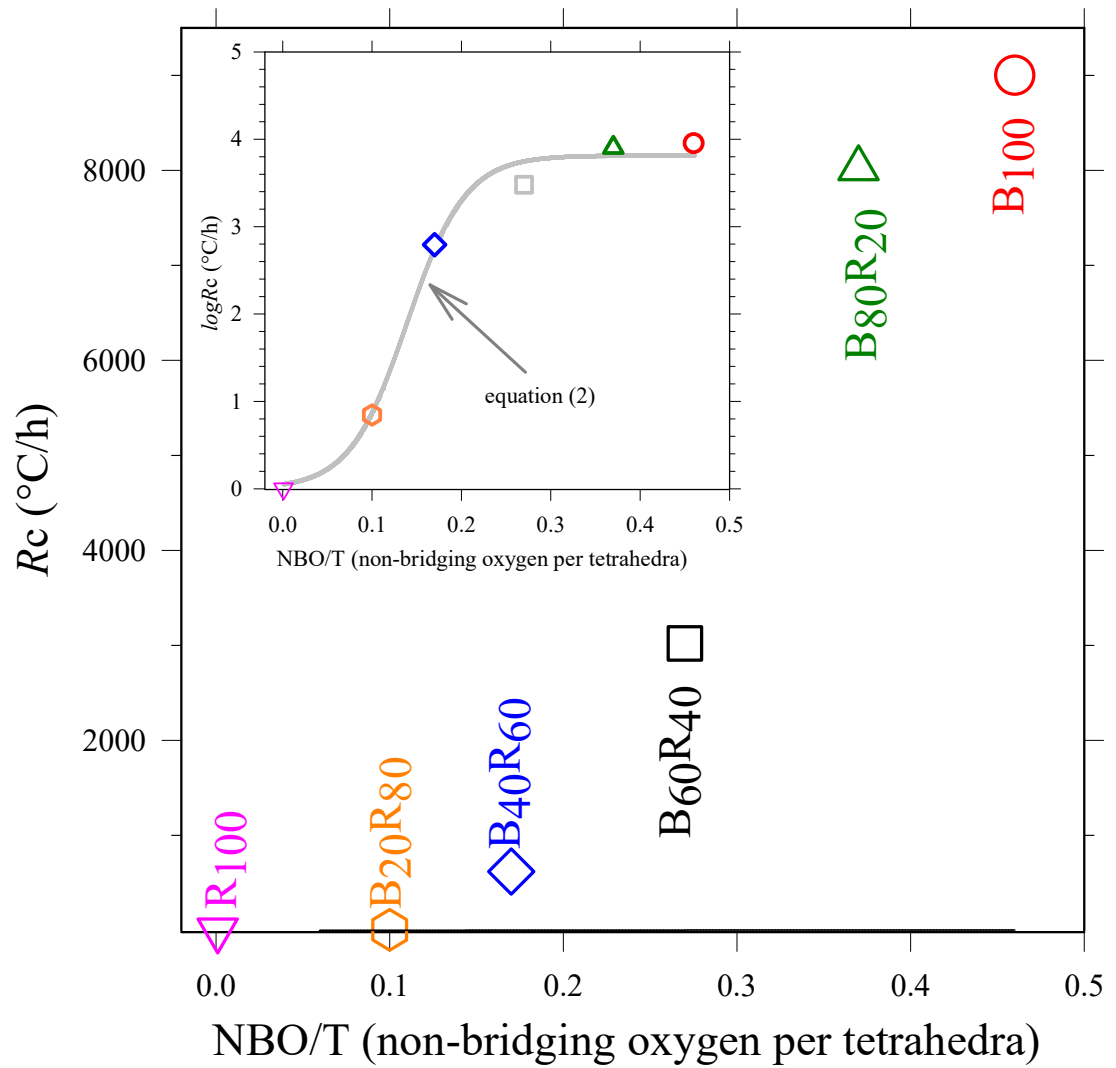
Figure 9. *Rc vs* NBO/T (R_{100} to B_{100}). The inset shows the critical cooling rate in a log scale with the fitting of equation 2.
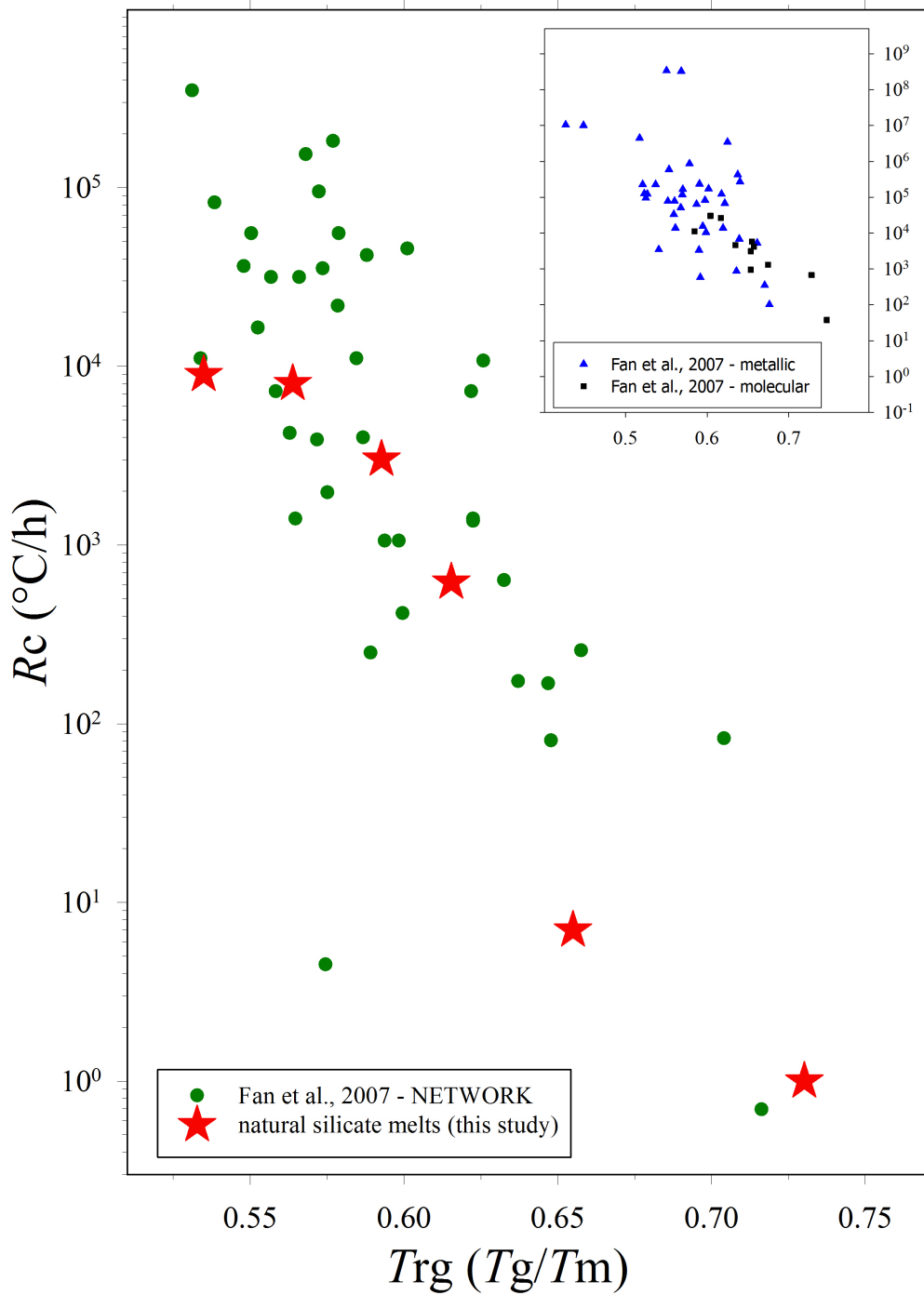
Figure 10. Trg *vs* Rc of sub-alkaline silicate compositions compared with metallic, molecular and network glass-forming liquids (Fan et al., 2007). The red line is a guide for eye, whereas the quantitative relationship between Trg *vs* Rc is reported in the text (equation 3).
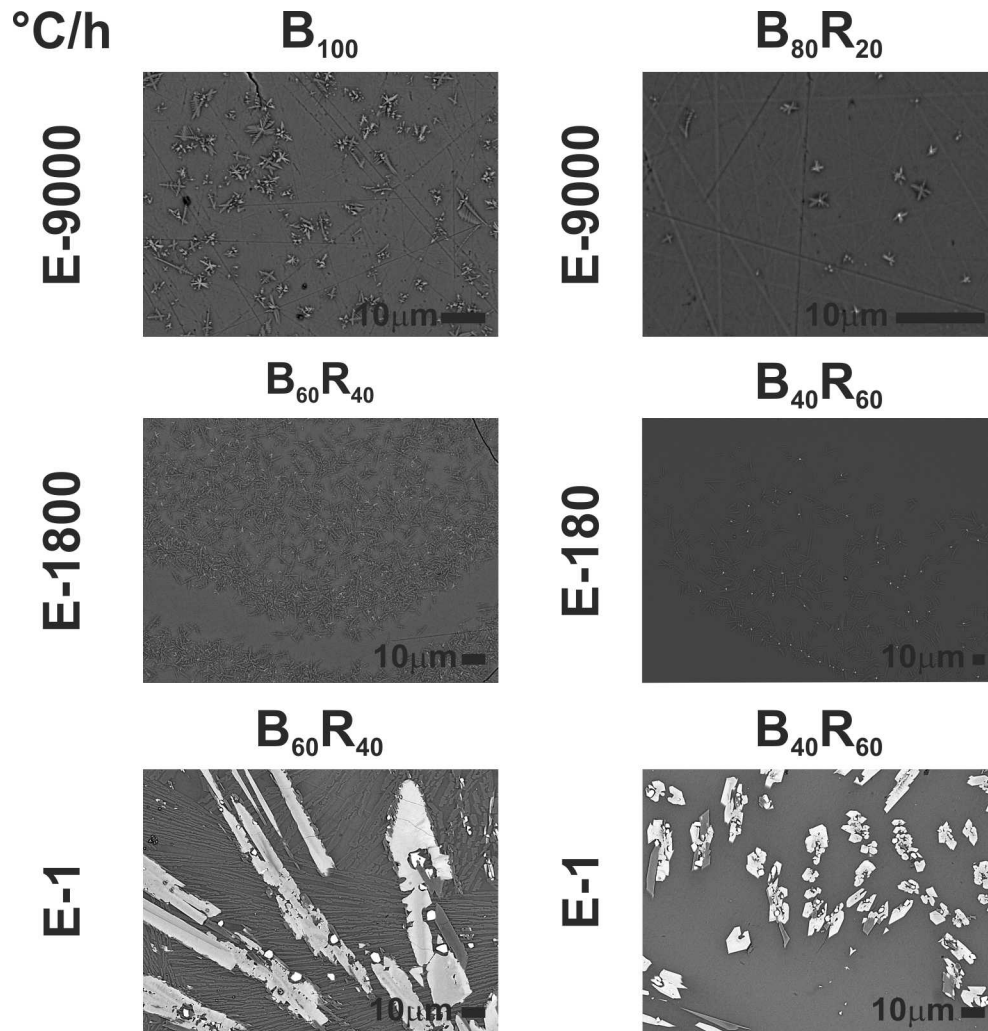
Figure 11. Examples of run-products with textures indicative of heterogeneous crystallisation of cpx on sp (top and middle rows) and of plg on cpx (bottom row).
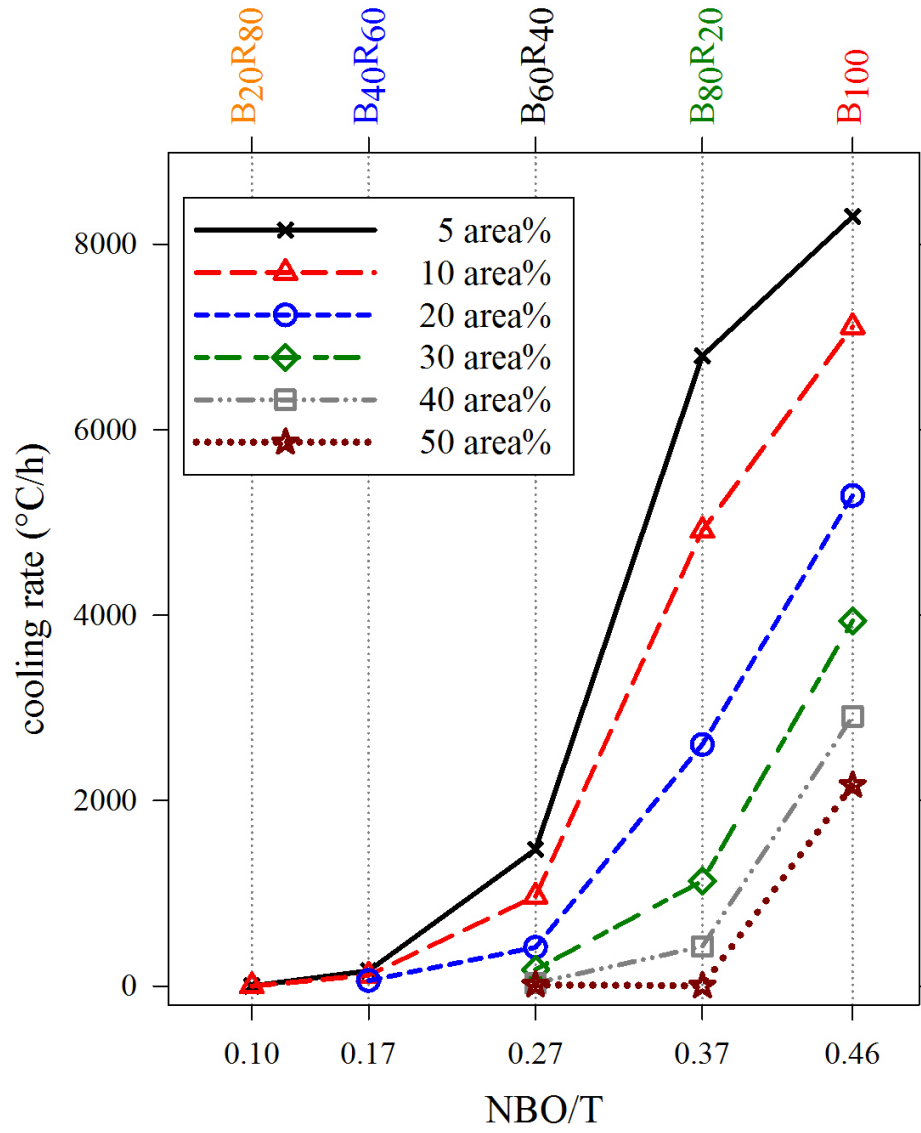
Figure 12. Relationships among NBO/T (and bulk composition), cooling rate and amount of crystals.
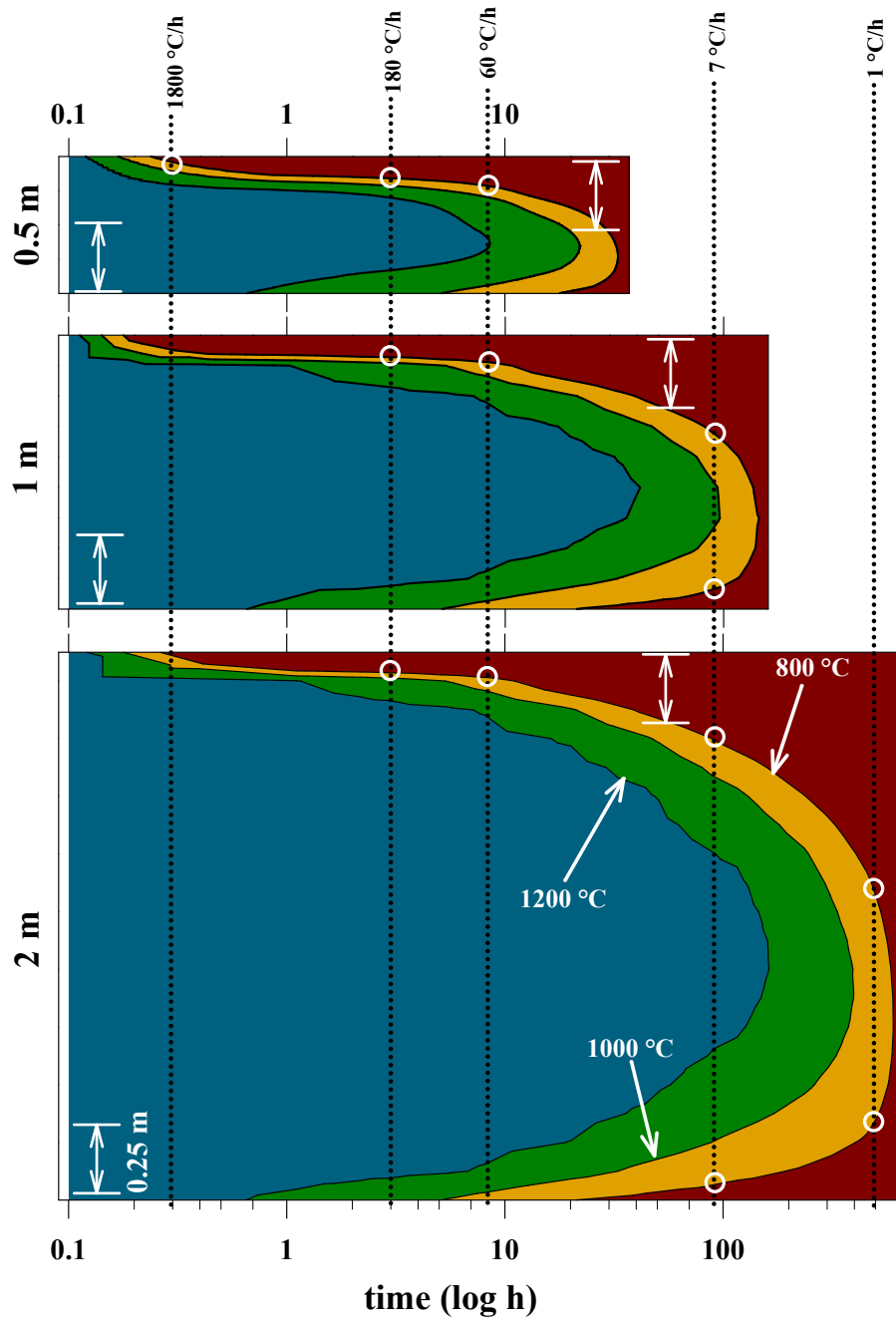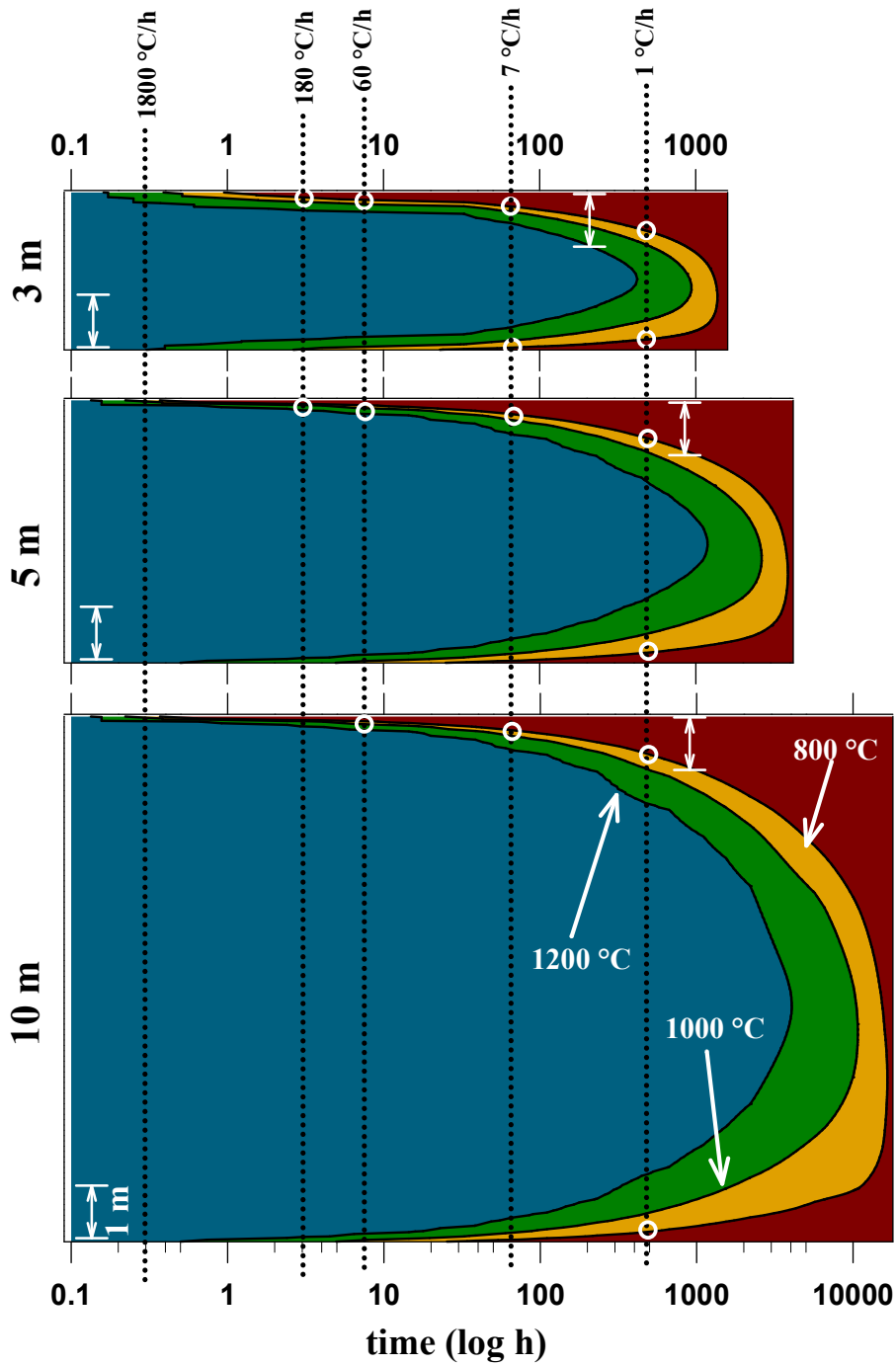
Figure 13a.

Figure 13b.

Figures 13. Simulations of cooling condition starting from 1300 °C and induced by conductive heat dissipation of silicate lavas with composition B_{100} and variable thickness; a) thickness of 0.5, 1 and 2 m; b) thickness of 3, 5 and 10 m. The blue, green, yellow and red areas indicate temperatures > 1200, 1200-1000, 1000-800 and < 800 °C, respectively.